

UNIVERSITY OF MARYLAND, COLLEGE PARK

Abstract

Faculty Name

Department of Astronomy

Doctor of Philosophy

**BETTII: A pathfinder for high angular resolution observations of
star-forming regions in the far-infrared**

by Maxime J. RIZZO

The Thesis Abstract is written here (and usually kept to just this page). The page is kept centered vertically so can expand into the blank space above the title too . . .

BETTII: A pathfinder for high angular resolution observations of star-forming
regions in the far-infrared

by

Maxime J. Rizzo

Dissertation submitted to the Faculty of the Graduate School of the
University of Maryland, College Park in partial fulfillment
of the requirements for the degree of
Doctor of Philosophy
2016

Advisory Committee:

Professor Lee G. Mundy, Chair/Advisor
Dr. Stephen A. Rinehart, Co-Advisor
Professor Andrew Harris
Dr. Mark Wolfire
Dr. Alison Nordt

To Michelle, my parents, and my brother.

Acknowledgements

The acknowledgments and the people to thank go here, don't forget to include your project advisor...

Contents

Acknowledgements	iii
Contents	v
List of Tables	vii
List of Figures	ix
List of Abbreviations	xi
Physical Constants	xiii
List of Symbols	xv
I Star formation in clustered environments	3
1 Molecular Clouds	3
2 Star formation	5
2.1 Standard models	5
2.1.1 Gravitational collapse	5
2.1.2 YSO classification and characteristics	8
2.2 Mass accretion in clusters	12
3 Dust as a tracer of star formation	14
3.1 Dust populations and properties	15
3.2 Basics of dust extinction	17
3.3 Radiative transfer modeling	19
3.4 Observing star formation	20
II Star Formation in Clustered environments with SOFIA FORCAST	23
1 Introduction	23
2 Sample description and scientific goals	24
3 Observations	26
4 FORCAST characterization	28
4.1 PSF size	29
4.2 Aperture correction factor	31
4.3 Instrument response and overall uncertainty	32
5 Data reduction and photometry	34
5.1 Pre-treatment	34
5.2 Source flux extraction	35

5.3	Image sensitivity	36
5.4	Other photometry	38
6	Data products	40
6.1	Mosaics	40
6.2	Photometry and SEDs	41
6.3	Fitted physical parameters and sample statistics	45
7	SED fitting	46
7.1	A custom grid of models	46
7.2	Fitting method	50
7.3	Overview of derived parameters	51
7.4	Estimating parameter uncertainty	51
7.5	Discussion	51
8	Application to two clusters	55
8.1	IRAS20050+2720	57
8.1.1	Context	57
8.1.2	Observations and discussion	58
8.2	NGC 2071	65
8.2.1	Context	65
8.2.2	Observations and discussion	68
9	Conclusion and future work	70

List of Tables

II.1	List of desired sensitivities	26
II.3	List of targets	28
II.5	SOFIA photometry comparison	37
II.7	FORCAST Sensitivities	37
II.9	Spitzer photometry comparison	39
II.11	NGC1333 photometry	44
II.13	SED model grid	48
II.15	Hyperion simulation parameters	49
II.17	Fitted parameters	54
II.19	Source fluxes in IRAS 20050+2720's dense core	58
II.21	Clustered sources in IRAS20050+2720's dense core	66
II.23	Sources in NGC2071's dense core	70

List of Figures

I.1	Early evolution of YSOs	10
I.2	Late evolution of YSOs	11
I.3	Scenarios of clustered star formation	14
II.1	Saturation and confusion	24
II.2	PSF size	30
II.3	PSF size of calibrators	31
II.4	aperture correction	32
II.5	Instrumental response	33
II.6	RGB images of select sample of sources	41
II.7	NGC1333 SEDs	42
II.8	Ophiuchus SEDs	43
II.9	Spectral Index distribution of point sources	45
II.10	Fitted envelope mass and luminosity distribution	52
II.11	Estimated luminosity vs bolometric luminosity	52
II.12	Luminosity excess as a function of envelope mass	53
II.13	Mass versus spectral index	53
II.14	Inclination versus mass	55
II.15	Luminosity versus spectral index.	55
II.16	NGC2071 and IRAS20050+2720	56
II.17	37 μ m observations of the IRAS 20050+2720 core, with the 5 identified objects. The blue contours are from a 2.7 mm continuum emission observed by the OVRO array (Beltrán et al., 2008) at levels from 10 to 46 mJy beam $^{-1}$ by increments of 4 mJy beam $^{-1}$. The resolution of the 2.7 mm beam is $\sim 4.8''$, while the r.m.s noise is 1.5 mJy beam $^{-1}$. The dashed line is the axis of a bipolar outflow identified by Bachiller, Fuente, and Tafalla (1995). The beam shown at the bottom left represents the resolution of the FORCAST instrument.	59
II.18	The core of IRAS20050+2720 is seen in the four bands of the <i>Spitzer</i> IRAS instrument, as well as with the four FORCAST bands. The increased resolution of FORCAST compared to previous instruments allows to match the long-wavelength emission with its short wavelength counterpart. The stretch in each image is adjusted for optimal readability. The white contours correspond to the FORCAST 37 μ m emission [mention the contour levels].	62
II.19	IRAS20050+2720 SEDs	64

II.20 The core of NGC2071 is seen in two bands of the *Spitzer* IRAC instrument ("I1" and "I4"), as well as with the four FORCAST bands. The increased resolution of FORCAST compared to previous instruments allows to match the long-wavelength emission with its short wavelength counterpart. The stretch in each image is adjusted for optimal readability. The white contours correspond to the FORCAST 37 μm emission [mention the contour levels]. 69

List of Abbreviations

LAH List Abbreviations Here
WSF What (it) Stands For

Physical Constants

Speed of Light $c_0 = 2.997\,924\,58 \times 10^8 \text{ m s}^{-1}$ (exact)

List of Symbols

a	distance	m
P	power	W (J s ⁻¹)
ω	angular frequency	rad

Introduction

In order to improve the mind, we ought less to learn, than to contemplate.

R. Descartes

The work presented in this thesis is centered around the design, development, and testing of an astronomical balloon-borne telescope called BETTII: the Balloon Experimental Twin Telescope for Infrared Interferometry. Developed at NASA Goddard Space Flight Center, this instrument is exploring a new observation technique called "Double-Fourier" interferometry, which could lead to future space-borne telescopes with very high angular resolution in the far-infrared regime. Various fields in astronomy would benefit from such enhanced capability, as demonstrated by the success of far-infrared single-aperture telescopes such as *WISE*, *Spitzer* and *Herschel*.

More than just a pathfinder, BETTII is a scientific instrument in its own right. For its first flights, it will study regions of clustered star formation with unprecedented details, providing almost an order of magnitude better spatial resolution than any existing or past far-IR facility.

This work describes some aspects of my involvement with BETTII as well as my contributions to the scientific field of clustered star formation using the only existing far-IR facility, SOFIA. The document is organized as follows:

- Chapter I describes the framework and current understanding of how stars are forming in clusters, and lays out the key tools that we use to study these regions.

- Chapter II is a study of nearby star-forming clusters using new data that we obtained with the SOFIA observatory. SOFIA offers moderately high angular resolution, which we attempt to use to improve the study of the brightest, densest regions of star formation. This work is to be submitted for publication shortly after the conclusion of this dissertation.
- Chapter ?? describes the physical principles of interferometry which drive the design of the balloon instrument. We predict the sensitivity of the instrument and identify scientific targets and calibrators that are suitable for our first flights.
- Chapter ?? is a standalone, refereed publication that was published in 2015 on the spectral sensitivity of double-Fourier interferometers in general. It proposes a mathematical framework to analyze the sensitivity of such instruments to various types of noise sources. We apply those findings to the case of BETTII.
- Chapter ?? discusses the design of the control system for BETTII, which presents unique challenges compared to any other balloon-borne instrument. We also discuss the controls algorithm that is used in flight to properly estimate the orientation of the payload, a key requirement to achieve successful interferometry.
- Chapter ?? shows results of the implementation that we discuss in the previous chapter. This consists of laboratory and on-sky testing of the observatory. We discuss the expected performance at float.
- Chapter ?? summarizes our findings and discusses the path forward for the BETTII project.

Chapter I

Star formation in clustered environments

1 Molecular Clouds

Molecular clouds are the dense regions of the interstellar medium (ISM) where stars are forming. They contain about half the mass of the ISM in $< 2\%$ of its volume (Ferrière, 2001). High densities ($n > 100 \text{ cm}^{-3}$) of mostly molecular hydrogen and low temperatures ($< 20 \text{ K}$) distinguish molecular clouds from the various other components of the ISM in galaxies: the Warm Neutral Medium (WNM), the Warm Ionized Medium (WIM), and the other cold phase of the ISM, the Cold Neutral Medium (CNM), which is thought to be the parent region in which molecular clouds are formed (Kennicutt and Evans, 2012). In addition to molecular hydrogen, molecular clouds also contain Helium (10% by number), dust ($\sim 1\%$ by mass), CO ($\sim 1 \times 10^{-4}$ by number), and traces of many other molecules.

Observations of molecular clouds reveal that they are highly structured with often a filamentary pattern [cite shaye?]. While the literature proposes multiple classifications for the various structures found in molecular clouds, we choose to focus only on two structures

which are key to this work: clusters, which are more local associations of stars in virial equilibrium (Lada and Lada, 2003); and dense cores, which are sites where stars form individually or in systems of small multiples (Williams, Blitz, and McKee, 2000). Clusters are formed of multiple cores, but cores can also be found outside of clusters, in the field. In the classical picture, clouds are thought to fragment into clusters, which still contain many times the Jeans' mass - the minimum mass for gravitationally-bound cores (Larson, 1994) which are also called prestellar cores (Di Francesco et al., 2007).

Approximately 60% of all stars are thought to form in embedded, young stellar clusters of 1-3 Myr with 100 or more stars (Porras et al., 2003; Allen et al., 2007). These >100 star clusters have characteristic sizes of 2-4 parsecs (pc) with peak surface densities of 100-1000 stars per square parsec and a typical median distance between nearest neighbor young stellar objects (YSOs) of 0.03 to 0.06 pc (Gutermuth et al., 2009).

Because star-forming clusters are surrounded by interstellar matter from the parent molecular cloud, they usually cannot be studied at optical wavelengths, due to the large obscuration from dust grains along the line of sight. Infrared observations can be used to probe these structures since the dust can acquire sufficient temperature to emit thermally from the mid-infrared to millimeter and radio wavelengths.

The high density of YSOs within clusters, combined with their typical separations of few hundredths of parsecs requires a high angular resolution in order to capture the relevant spatial scales at which accretion mechanisms are occurring to give the star its final mass.

2 Star formation

2.1 Standard models

A considerable amount of literature exists on star formation and the various physical processes involved in forming stars. In this section, we review some of the most standard views that describe how stars are born and grow to acquire their final masses.

2.1.1 Gravitational collapse

A simple way to derive characteristic quantities related to the formation of stars is to consider a pre-stellar core as a spherical clump of uniform, isothermal gas in hydrostatic equilibrium. For such a system, the Virial theorem applies, which describes the balance between the gravitational potential and the kinetic thermal energy within the gas. In other words, in hydrostatic equilibrium, the core's self-gravity is compensated by the internal pressure caused by the temperature of the gas. For the same radius and temperature, a core with more mass will lead to a runaway collapse. While simplistic, this treatment leads to a handy derivation of critical timescales, sizes, and masses that form a good starting point for more elaborate theories.

First, it is important to determine what are the characteristic timescales of star formation. In the core with a uniform density, the simplest timescale to define is called the free-fall time: this is the time it takes for the total gravitational collapse of a spherically-symmetric clump of uniform density ρ if only the force of gravity is considered:

$$t_{\text{ff}} \sim \left(\frac{3\pi}{32G\rho} \right)^{-1/2} \sim 2 \times 10^5 \text{ yr} \left(\frac{\rho}{10^{-19} \text{ g cm}^{-3}} \right)^{-1/2}, \quad (\text{I.1})$$

where we have substituted a typical value for the gas density in clusters. The free-fall time is usually a lower limit on the collapse timescale, since there will always be some thermal pressure that will resist gravity and slow down the infall of gas into the potential well.

The other relevant quantity that involves time is the sound speed in the cloud, $c_s = (kT/(\mu m_H))^{1/2}$, where μ is the mean molecular weight of the gas and m_H the mass of hydrogen. For a given spatial scale R , the sound-crossing time is defined as $t_s = R/c_s = 4.9 \times 10^5 \text{ yr} \left(\frac{R}{0.1 \text{ pc}} \right) \left(\frac{c_s}{0.2 \text{ km s}^{-1}} \right)^{-1}$. This is the time it takes for a wave to cross the scale R while traveling at the sound speed. Intuitively, if the core has a size R such that $t_{\text{ff}} < t_s$, it will tend to collapse faster the gas in the cloud can compensate to maintain hydrostatic equilibrium. This corresponds to a characteristic sizescale that is called the Jeans' length, and corresponds to the characteristic sizescale of gravitational instability within a cloud (McKee and Ostriker, 2007):

$$\lambda_J = c_s \times t_{\text{ff}} = 0.04 \text{ pc} \left(\frac{c_s}{0.2 \text{ km s}^{-1}} \right) \left(\frac{\rho}{10^{-19} \text{ g cm}^{-3}} \right)^{-1/2}. \quad (\text{I.2})$$

The Jeans mass is the amount of mass within a sphere of diameter λ_J , and corresponds intuitively to the minimum mass a core needs to gather in order to trigger an gravitational collapse:

$$M_J = \frac{4\pi}{3} \rho \left(\frac{\lambda_J}{2} \right)^3 \quad (\text{I.3})$$

$$= 0.06 M_\odot \left(\frac{c_s}{0.2 \text{ km s}^{-1}} \right)^3 \left(\frac{\rho}{10^{-19} \text{ g cm}^{-3}} \right)^{-1/2} \quad (\text{I.4})$$

Note that this formalism completely ignores the material that surrounds the core while it collapses. In practice, the cloud exerts an external pressure on the core that needs to be taken into account when calculating the critical masses. This more elaborate case

of a clump of self-gravitating gas on the verge of collapse that is immersed in a medium of external pressure P_{ext} is called a Bonnor-Ebert sphere. It can be shown (McKee and Ostriker, 2007) that the sizescale is similar to the Jeans' length, and the mass scale is a few times smaller than the Jeans' mass, which stays well within the accuracy limits of our simple model.

Once the gas starts its gravitational collapse, nothing stops it until the central pressure and density reach values that trigger the ignition of nuclear fusion. This is the birth of the star. This new mechanism creates a large amount of radiation pressure that balances out the collapse and forms a new hydrostatic equilibrium.

In practice, it is likely that a single core fragments into multiple centers of collapse, each of them exceeding the local Jeans mass. This would create systems of binaries or small multiples instead of single stars, a scenario that is currently favored [LARSON?].

In the standard model, the collapse begins at the center of the core and propagates outward at the sound speed, so the density structure of the initial core will change as a function of time. Most models result in an infalling envelope with density profiles which follow power laws from $r_{\text{env}}^{-1.5}$ to r_{env}^{-2} , an important observable that can be useful to test these theories. Some models of slowly-rotating infalling clouds suggest more complex density profiles for the envelopes (e.g. Ulrich, 1976; Terebey, Shu, and Cassen, 1984) than simple power laws, but are observationally difficult to constrain due to the small differences with traditional power-law envelopes and the small scales at which those differences occur (a few 100's of AU).

Through conservation of angular momentum, some of the surrounding material naturally flattens into a centrifugally-supported flaring disk before it is fed to the star, and a bipolar cavity opens along the rotation axis of the system. The cavity opening can also be

bolstered by mechanisms such as stellar winds and jets [REFERENCE].

The object now has three characteristic components: the star itself; the flattened disk; and a diffuse envelope with an open cavity, which constitutes a mass reservoir for future accretion onto the star.

The accretion rate represents the speed at which the mass is transferred between different objects, and are important to set relevant timescales and to relate observables to the physics. For relatively low-mass star formation, the usually adopted accretion mechanism is called Shu accretion (“Self-similar collapse of isothermal spheres and star formation” 1977), and predicts a mass accretion rate of the envelope onto the disk $\dot{M}_{\text{env}} \propto c_s^3/G$, where c_s here represents the sound speed that includes turbulence, and G is the gravitational constant. Typical accretion rates for $c_s \sim 2.7 \text{ km s}^{-1}$ are $\dot{M}_{\text{env}} \sim 4.8 \times 10^{-6} M_{\odot} \text{ yr}^{-1}$ (Dunham et al., 2010).

Although most of the mass is contained in the H₂ gas, there is a small fraction of material in the form of dust grains of various sizes and populations. Despite their low mass, these grains play a very important role in determining the observable properties of YSOs, because of their tendency to absorb short wavelengths and radiate in the thermal infrared (see Section 3).

2.1.2 YSO classification and characteristics

We have determined that YSOs are composed of a star, a disk, and an envelope. The star is believed to be fairly well understood as a young object in hydrostatic equilibrium on its way to the main sequence. Depending on many parameters, the spatial distribution of gas in the disk and the envelope can be predicted by simple models, but in all likelihood is

very complex, inhomogeneous, and asymmetric. For clarity, we will discuss here the simple models that can be used to describe the YSOs in the multiple stages of their evolution.

In the most common model of the evolution of young stars, there are four stages in the lifetime of a YSO. The first stage consists of a dense core right after the YSO is born. The disk is almost nonexistent, the envelope still is dense and circularly symmetric. This is called Stage 0. As the system evolves, the cavity opening angle grows, the density of the envelope decreases, and the size of the disk increases. When a YSO is Stage III, both the disk and the envelope are almost entirely depleted.

The various stages of YSO (from 0 to III) have very distinct observational signatures, although are highly dependent on the viewing angle. The most commonly used tool to classify YSOs based on their SEDs is to use the spectral index, which corresponds to the mid-IR slope α in the log-log plots, with $\alpha = d(\log \lambda F_\lambda)/d \log \lambda$ between 2 to 20 μm (McKee and Ostriker, 2007). The four classes of YSOs are:

- Class 0: Most the of short-wavelength ($< 10 \mu\text{m}$) light is highly obscured by the dust in the massive envelope. Most of the emission is around $100 \mu\text{m}$ and into the sub-millimeter/radio regimes. If there is a disk, it is very small. Some authors (Dunham et al., 2010) classify a source as Class 0 as long as the amount of the mass in the envelope is at least half the total mass.
- Class I: Light scatters at short wavelength off the dust grains to give us a hint at the embedded object, but it still very obscured. The envelope's mass is lower, and the disk extends to larger distances. The typical spectral index α is positive.
- Class II: The YSO is now a pre-main sequence star, with a spectral index $-1.5 < \alpha < 0$ a significant circumstellar disk. This is traditionally referred to as a classical

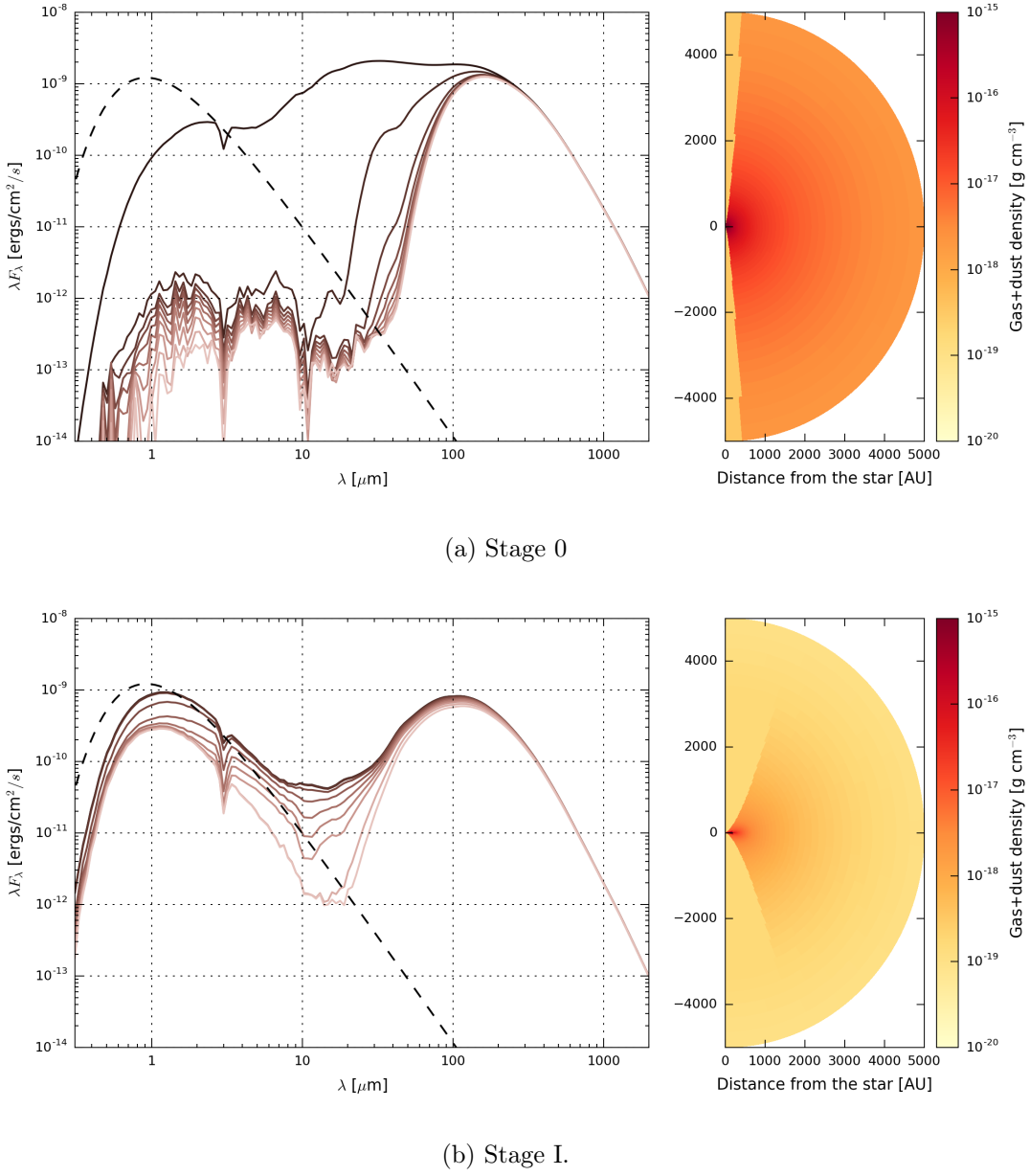


FIGURE I.1: Early evolution of YSOs.

T-Tauri star.

- Class III: Still a pre-main sequence star, but most of the accretion has stopped, and $\alpha < -1.5$. The envelope has almost completely disappeared, and so has most of the disk.

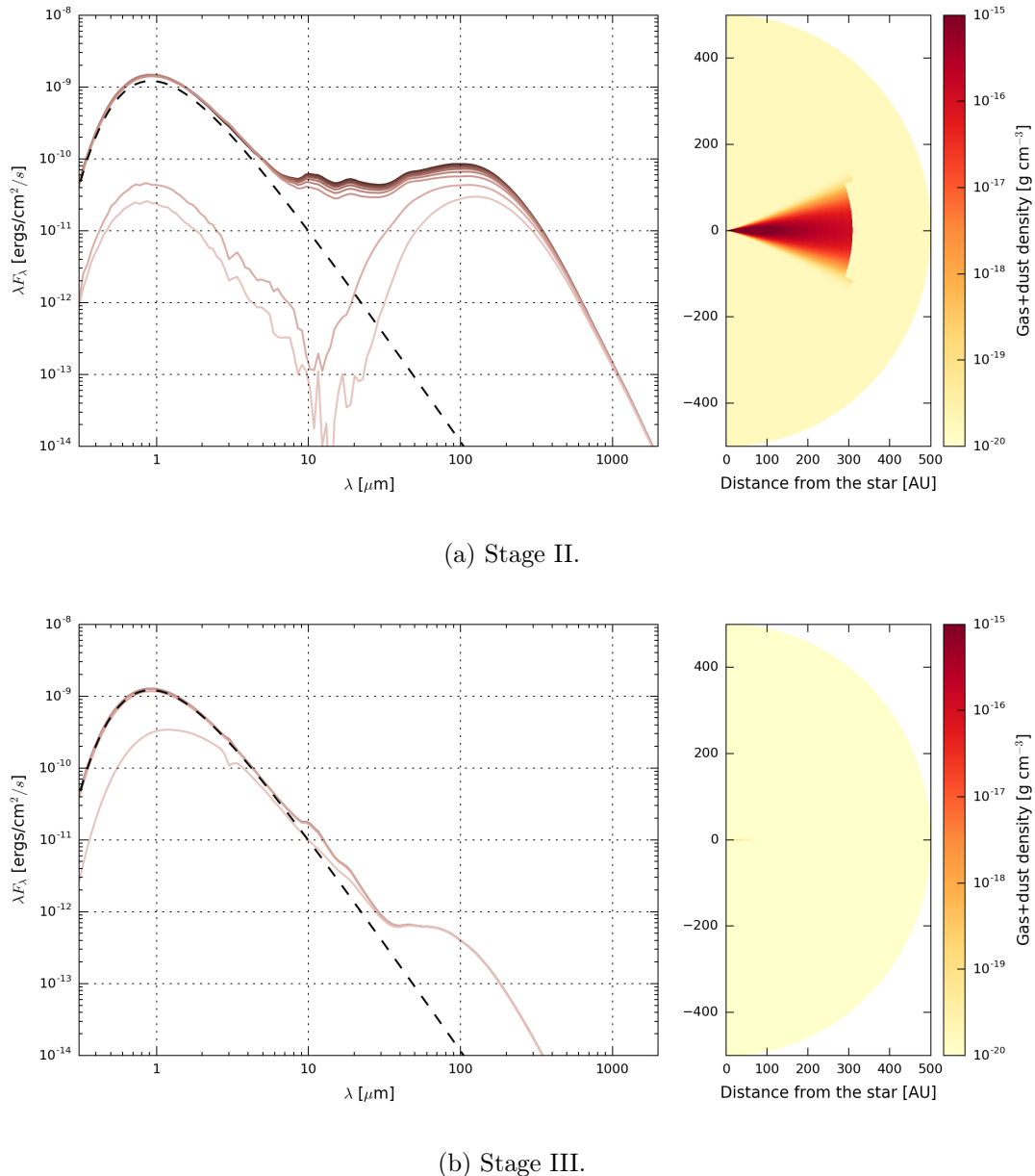


FIGURE I.2: Late evolution of YSOs.

An illustration of canonical spectral energy distributions (SED) and density structure is shown in Figs. ?? for the four main stages, with parameters taken in Whitney et al. (2003b). On the left of each picture, the SED is the measurable quantity when the YSO is unresolved at all wavelengths. The challenge is to estimate the density structure (to the right) by measuring the SED. The different lines plotted in the SEDs are different inclination angles, highlighting the enormous impact of the viewing angle on the potential interpretation of these SEDs. The dashed line corresponds to the Planck function from the central source. These models were run using the Hyperion software (Robitaille, 2011) with "OH5" dust (Ossenkopf and Henning, 1994), as discussed in more details in Section 3.

These SEDs are often characterized and classified with standard observational metrics, such as the bolometric temperature and luminosities (Myers and Ladd, 1993; Dunham et al., 2010):

$$L_{\text{bol}} = 4\pi d^2 \int_0^\infty S_\nu d\nu, \quad (\text{I.5})$$

$$T_{\text{bol}} = 1.25 \times 10^{-11} \frac{\int_0^\infty \nu S_\nu d\nu}{\int_0^\infty S_\nu d\nu} \text{ K}, \quad (\text{I.6})$$

where S_ν is the flux density in $\text{W m}^{-2} \text{Hz}^{-1}$.

2.2 Mass accretion in clusters

The discussion in the previous section represents a canonical view of how a single core collapses and forms a star. While it is convenient to assume that the original core forms a fixed reservoir of gas that will determine the star's final mass, it is likely too simplistic, since these YSOs are preferentially forming inside of clusters close to multiple other YSOs

and sharing a dense, often turbulent environment (Porras et al., 2003; Allen et al., 2007; Gutermuth et al., 2009).

The question of how stars acquire their final mass is key in studying star formation. Does dense gas fragment into isolated centers of collapse? Do young stars competitively accrete material from a surrounding common reservoir? Do gravitational interactions between forming young objects play a significant role in setting the final stellar mass function? Better observational understanding of these clusters is necessary to address these questions and to discriminate between the different models, as noted by Bonnell and Bate (2006), Offner and McKee (2011) and Myers (2011).

Given the typical stellar separations in clusters with fully formed young stellar objects and the typical densities of gas in these cores, 1000's of astronomical units (au, $1 \text{ pc} = 206\,265 \text{ au}$) are the size scales over which forming stars must draw material to become $0.5\text{-}10 M_{\odot}$. Once the material is inside 100 au, it is strongly bound to the forming stellar system (which may be one or more stars) and its fate is determined. To give an idea of the possibilities for accreting material, Fig. I.3 sketches three scenarios for how stars could capture mass in the cluster environment: core collapse, competitive accretion, and collisional merging. In core collapse (CC) (Fig. I.3a, McKee and Tan, 2003; Myers, 2011), the cluster's gas fragments into cores which collapse individually to form single, binary, or small multiple star systems; the available mass is defined by the original fragment. In competitive accretion (CA) (Fig. I.3b, Bonnell et al., 1997), the initial core collapses but contains a small fraction of the star's final mass; additional mass is captured competitively with other forming stars from the surrounding dense core gas. In collisional merging (CM) (Fig. I.3c, Bonnell and Bate, 2002), the initial fragments interact gravitationally and form larger mass cores before and during the formation process.

Are all these processes observed at once in star forming clusters? What conditions favor one versus the other, and why? Are these processes observed at different stages in the cluster's history?

Recent studies by Offner and McKee (2011) and Myers (2011) compared protostellar luminosity distributions with predictions of models based on these ideas. Offner and McKee (2011) suggest that both CC and CA could work if the star formation rate in the cluster increases with time; (Myers, 2011) finds that a CA-type model with additional Bondi accretion to produce massive stars works best. As highlighted at the end of the Offner and McKee (2011) paper, larger cluster samples and better data on massive stars are needed to improve the observational constraints on models.

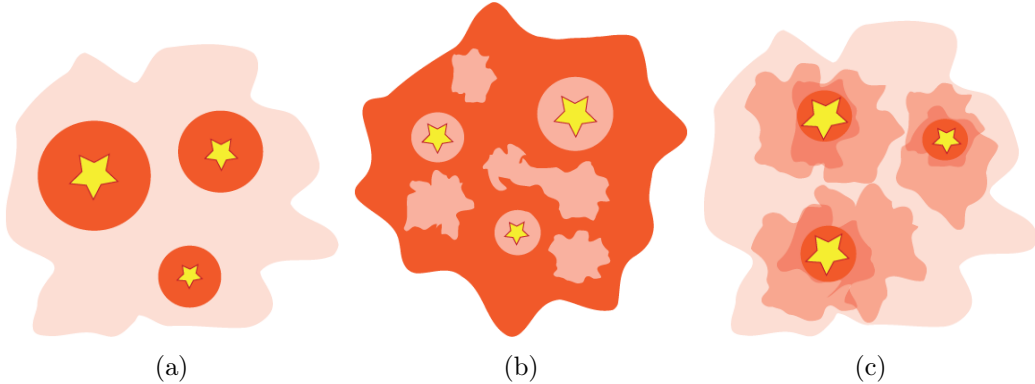


FIGURE I.3: Three scenarios of clustered star formation. Darker colors indicate higher densities.

3 Dust as a tracer of star formation

Despite being a small component by mass, interstellar dust is an important component of galaxies. Dust grains are heated up by absorbing the short wavelength emission from stars and re-radiate in the thermal infrared, accounting for $\sim 30\%$ of the total luminosity of the galaxy (Mathis, 1990).

Observationally, dust plays perhaps the most important role when it comes to studying star formation. It usually is assumed that dust is well mixed with the gas, which makes it an excellent tracer of the gravitational well and mass distribution in YSOs. Because H₂ and He molecules have very few spectral signatures, they are difficult to observe and study directly. Dust grains block UV and visible star light and emit continuum far-IR radiation, opening a large region of the electromagnetic spectrum for astronomers to study the properties of star formation. Alternative tools to study star formation are dedicated to observing spectral lines of the molecular compounds of the ISM such as CO and other dense gas tracers, a prospect that limits the study to the most dense regions since these compounds typically freeze out onto the surface of dust grains for sufficiently high densities [REF?]

3.1 Dust populations and properties

Perhaps the first understanding of the composition of dust grains in the ISM was described by Mathis, Rumpl, and Nordsieck (1977), where they studied the absorption spectrum of the diffuse ISM, and found that the measurements were appropriately fitted with a dust grain composition of silicates and small graphite particles (Stecher and Donn, 1965). They were able to fit the observed extinction curve with canonical grain-size distribution, typically $n(a) \propto a^{-3.5}$, where a is the grain size (assuming spherical grains) and $n(a)$ corresponds to the number of grains of sizes $< a$. This assumes low and high cutoffs for the grain sizes, typically 50 Å and 0.25 μm, respectively.

This grain-size distribution model was later on enhanced by Cardelli, Clayton, and Mathis (1989) to account for the difference in interstellar extinctions (hence size distributions) across different galactic lines of sight. These authors were able to successfully

parameterize this size distribution using a single parameter, R_V , which is the ratio of the total extinction $A(V)$ to selective extinction¹ (or color) $E(B-V) = A(B) - A(V)$. Smooth distributions of sizes of graphite and silicate grains between the less dense regions of the ISM, where $R_V = 3.1$, and the dense clusters, where $R_V = 5.3$ (Kim, Martin, and Hendry, 1994).

Observations in the thermal infrared from space telescopes have detected strong absorption lines at $9.7\text{ }\mu\text{m}$ and $18\text{ }\mu\text{m}$ which are attributed to stretching mode of Si-O and bending mode of O-Si-O, confirming the presence of silicates in dust compositions (Weingartner and Draine, 2001). Other emission features at 3.3 , 6.2 , 7.7 , 8.6 , and $11.3\text{ }\mu\text{m}$ (Sellgren, 1994) were attributed to bending and stretching modes of polycyclic aromatic hydrocarbons (PAH, see Gillett, Forrest, and Merrill, 1973; Allamandola, Tielens, and Barker, 1985), which are complex, planar organic molecules.

A consolidated model matching all-sky measurements by instruments on the COBE space observatory confirms the composition of amorphous silicates and carbonaceous grains with sizes ranging from large grains ($\approx 1\text{ }\mu\text{m}$) down to tens of atoms (Li and Draine, 2001), where the larger carbonaceous grains have graphitic properties and the smaller population have PAH-like properties.

[Molecular hydrogen is believed to form by recombination on the surface of dust grains [hollenbach and salpeter 1971, and are only able to survive from UV photodissociation within these obscured clouds.]

Knowing the dust composition and size distribution of grains is important to properly predict its observational behavior and relate it to the physical quantities of interest, since the goal of the exercise is to use dust as a tracer of star-forming mechanisms. A given

¹Extinction and colors are expressed in magnitudes

dust model needs to provide several key quantities that can be used in radiative transfer modeling (see Section 3.3), such as the albedo, the scattering function, and the opacity.

In the very cold regions surrounding a YSO, where the dust temperature typically never exceeds a few tens of K, it is expected that these dust grains are covered by a mantel of ices which can dramatically change their radiative properties, especially at short wavelengths.

3.2 Basics of dust extinction

Dust grains are responsible for the extinction within molecular clouds, inside of clusters, and also within each YSO; although these various extinctions could originate in different types of grain populations. The typical representation of this extinction uses the ratio of observed over expected flux, measured in V-band: $A_V \equiv A(V) = 2.5 \log(F_\nu^{\text{obs}}/F_\nu)$. The extinction, $A(\lambda)$, is a function of wavelength and is expressed in magnitudes. An alternative representation is to consider the extinction as being caused by an optical depth τ_{ext} such as $\exp(-\tau_{\text{ext}}) = F_\nu^{\text{obs}}/F_\nu$. We have the equivalence $A(\lambda) = 1.086\tau_{\text{ext}}(\lambda)$.

At sufficiently long wavelength, dust opacity models can usually be represented by a simple power-law, $\kappa_\nu = \kappa_0(\nu/\nu_0)^\beta$, with the index β depending on the specifics of the dust model. The opacity κ_ν is expressed in $\text{cm}^2 \text{g}^{-1}$, and can be interpreted as a extinction cross-section per unit mass. Most dust models assume a 1:100 dust-to-gas ratio, and derive opacities per unit gas+dust mass, instead of just dust mass. From a radiative transfer perspective, the observed specific intensity from a thermal source $B_\nu(T)$ in the optically thin regime is $I_\nu = \tau_\nu B_\nu(T)$, where the optical depth is $\tau_\nu = \kappa_\nu \int \rho_{\text{dust}} dl$. ρ is the density and the integral is calculated along the line of sight to the source.

A measure of the intensity from a source can thus lead to an approximation of the

total mass within a primary beam, for a given dust grain model. For a source with a measured sub-millimeter flux density S_ν , in the optically thin regime we can write $S_\nu = \tau_\nu B_\nu(T)\Omega$, where Ω is the solid angle of the source, $\Omega = A/d^2$, with A the area of the source and d its distance. We obtain a measure of the mass by writing $M \approx A \int \rho dl$, to obtain (Shirley et al., 2000):

$$M = \frac{S_\nu d^2}{B_\nu(T_{\text{dust}})\kappa_\nu}, \quad (\text{I.7})$$

with a dust temperature is usually taken to be between 10 to 20 K.

With only near- to far-IR wavelengths observations, however, it is more difficult to estimate the dust mass, because the system is usually not in the optically thin regime and very dependent on the local geometry and viewing angle. To use these observations, which are interesting because they naturally are at higher resolution than single-dish submillimeter data, detailed radiative transfer models are usually required (Section 3.3).

Dust grains can either scatter or absorb photons, and both of these processes have their own frequency-dependent efficiency. Large grains are usually considered in local thermal equilibrium (LTE), in which case the thermal emission balances out the absorption. However, small grains ($< 50 \text{ \AA}$) can be subject to stochastic heating, where single photons can heat up the grains to much higher temperatures for very short amounts of time. Scattering mechanisms can be much more complicated to represent, as they usually involve a scattering phase function, describing the deflection angle of incident photons (which also depends on wavelength). Most models show that dust grains are preferentially forward-scattering [CITE Draine?]. The scattering properties of the dust model exclusively influence the short-wavelength emission, while the absorption properties influence all wavelengths.

3.3 Radiative transfer modeling

Several radiative transfer codes exist in the literature, and we have explored a few of them. We opted for a recently-developed package called Hyperion (Robitaille, 2011), which is a Python interface to a 3D Monte-Carlo code by Whitney et al. (2013). The code is versatile, parallelized, can accept different dust models and can generate various types of geometries and density grids.

Hyperion functions in two steps. After choosing a discrete grid to represent a density model and adding energy sources, the temperature structure of the dust is calculated by propagating photon packets and determining the dust LTE temperature in each cell. Multiple iterations of this process are usually required to converge to a decent thermal structure.

Once the dust temperature is known, the dust becomes a source of thermal radiation. This type of radiation is modeled using ray tracing, which provides a very good signal-to-noise ratio (SNR). The light from the central source which was not absorbed, however, needs to be propagated and scattered off the dust grains, for example using a method called peeling-off (Yusef-Zadeh, Morris, and White, 1984). For non-isotropic scattering, this process has relatively low SNR, hence requires a lot of photons packets to function properly. While there are future plans to implement raytracing for scattering (Robitaille, 2011), we are currently forced to wait long times for simulating YSOs with massive envelopes because of this problem.

[Put models of YSOs with different masses here.]

These models usually present a large amount of degeneracies, especially when the entire range of wavelengths is not covered, as it is the case for most astronomical sources.

For example, an SED will look very different depending on the viewing angle. If we see down the throat of the cavity, the short-wavelength light from the central source will not exhibit a lot of extinction. If we observe this same source through the disk and envelope, these same wavelengths will show a lot of extinction. The short wavelength, up to the peak of the SED, are very geometry-dependent and highly degenerate parameters.

This realization helped us target our work using this code. Others (e.g Robitaille et al., 2006) have produced standardized grids of pre-computed models which randomly sample a very large number of source geometry parameters. These grids are routinely used by the community to fit a set of unresolved SED measurements at discrete wavelengths. However, most often the scatter in the parameters for the few best fit models prevents from drawing meaningful conclusions on the observations.

[Example?]

One of the key challenges of using this code is to determine which dust models to use. For this work, we choose to use exclusively OH5 dust (Ossenkopf and Henning, 1994), which represents grains with an ice mantle which are the result of a coagulation phase of an initial distribution of grain sizes following $n \propto a^{-3/2}$. This model was found to accurately represent some grain distribution in the ISM [NEED CITATION, CHECK OUT TRACY'S PAPER].

3.4 Observing star formation

In the past decade, space-based infrared observatories such as *Spitzer* and *Herschel* have really allowed the beginning of the detailed study of dust around forming stars, by sampling the SEDs in key spectral regions, such as the PAH region (with the IRAC instrument on

Spitzer), the mid-infrared (with the MIPS instrument, especially its 24 μm channel), and the far-IR (with the PACS instrument on *Herschel*).

However, these observatories lack the required angular resolution to observe the key physics of star formation in dense clusters in the key wavelength region between 30 μm and 200 μm. For a diffraction-limited single aperture telescope, the angular resolution and spatial resolutions R_θ and R_{linear} are:

$$R_\theta = 17.6'' \left(\frac{\lambda}{70 \mu\text{m}} \right) \left(\frac{D}{1 \text{m}} \right)^{-1}, \quad (\text{I.8})$$

$$R_{\text{linear}} = 0.04 \text{ pc} \left(\frac{d}{500 \text{ pc}} \right) \left(\frac{\lambda}{70 \mu\text{m}} \right) \left(\frac{D}{1 \text{m}} \right)^{-1}, \quad (\text{I.9})$$

which shows that even with *Herschel* and its 3.5 m primary mirror and its 70 μm channel, we can barely resolve clustered YSOs (typical separations of a few hundredths of pc), let alone study their structure in detail.

To further complicate the problem, most space observatories are tailored for very sensitive observations, so the brightest regions of clusters often cause saturation issues due to a lack of dynamic range. These two issues have continually prevented us from gathering a good picture of the physics in these dense and important regions of stellar birth.

[Image that shows the saturation/lack of resolution]

[Talk about SOFIA]

Chapter II

Star Formation in Clustered environments with SOFIA FORCAST

1 Introduction

Most stars in the Galaxy form in cluster environments of sizes 2-4 pc, often containing more than 100 young stellar objects (YSOs), with typical separations of <0.05 pc between stars near their centers (Porras et al., 2003; Allen et al., 2007; Gutermuth et al., 2009). Previous studies have been effective in elucidating the young stellar content and distribution in clouds on large scales (parsec down to 0.05 pc) (Kennicutt and Evans, 2012), but young cluster cores, born in dense portions of molecular clouds, are more difficult to observe. They are obscured at optical through near-IR wavelengths. At mid-IR through far-IR wavelengths, the material surrounding YSOs and involved in the stellar birth process emits due to heating by the young stars, but the resolution to date has not been sufficient to isolate individual stars in the cores of most nearby young clusters.

2 Sample description and scientific goals

Spitzer has tremendously helped our understanding of star formation, by providing sensitive observations in continuum bands from $3.6\text{ }\mu\text{m}$ to $160\text{ }\mu\text{m}$. In particular, the MIPS $24\text{ }\mu\text{m}$ channel provided a robust way to determine the spectral index of YSOs, hence leading to dramatic improvement of understanding of the YSO population in clusters (e.g., Gutermuth et al., 2009; Gutermuth et al., 2011).

However, the most dense regions of clusters still present a challenge for the MIPS instrument, as the YSOs are too bring and/or in too close proximity, which leads to saturation and confusion, as exhibited in Fig. ??.

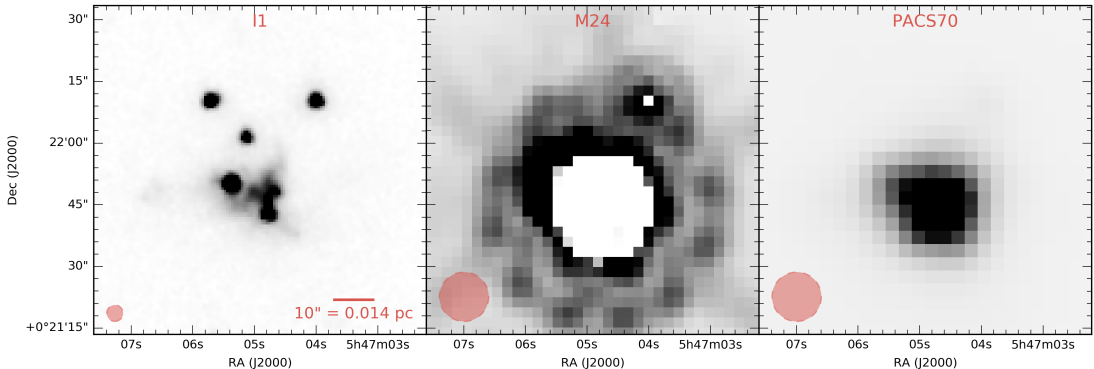


FIGURE II.1: Saturation and confusion in NGC2071.

BETTII will tackle the confusion problem at wavelengths from 30 to $100\text{ }\mu\text{m}$, and will be complementary to *Herschel* observations of star-forming regions. SOFIA, however, can already start studying these dense regions with its FORCAST instrument, providing $2\text{-}3.5''$ resolution between 10 and $37\text{ }\mu\text{m}$.

We responded to SOFIA FORCAST's first science call with a proposal for a survey of nearby star-forming cluster cores. The clusters were selected from a list of dense young clusters within 1 kpc of the Sun based on Porras et al. (2003) and Gutermuth et al. (2009).

From this list we selected clusters that were: (1) north of -25 degrees declination so that they could be done from a northern hemisphere flight; (2) included membership of >50 YSOs; and (3) included bright 8-24 μm sources within the dense cores based on *Spitzer* and/or WISE data.

In order to sample the most range of the SED, we proposed to observe in 4 of FORCAST's science continuum bands: 11.1, 19.7, 31.5 and 37.1 μm . This wavelength coverage would be very complementary to archival data from *Spitzer* and WISE. Our focus on bright regions spread all across the sky is convenient for SOFIA, and our project would be observed as a gap-filler during the primary science flight legs.

The main objective of the survey is to gather statistics and fill the SED gap between *Spitzer*'s bands and *Herschel*'s bands. *Spitzer* is often unusable for these targets because of saturation and confusion, and *Herschel* is confused as well. As it is often the case, *Herschel* observations were not available for our targets, making these SOFIA observations the best attempt at observing those regions at mid-IR wavelengths, and our only opportunity to constrain the SED of very clustered YSOs in these regions to infer their physical properties.

Our strategy was successful and we were awarded time during the first and second science cycles of FORCAST (see Tab. II.3). The data analysis and scientific interpretation is presented in the next few sections. First, we describe our observations, as well as the archival datasets that we use to complement our observations. Second, we properly characterize the systematics of the FORCAST instrument and their variations over multiple science flights spanning multiple years. The data reduction process is then explained, followed by a snapshot of the data products themselves. We then discuss our SED fitting strategy, and fit the SEDs of three of our clusters to derive the physical properties of their embedded YSOs.

3 Observations

The FORCAST camera has two separate 256×256 pixel infrared arrays that cover the wavelength range from $5.5\text{-}37\,\mu\text{m}$ in multiple bands with $0.768'' \times 0.768''$ pixels. The two arrays can observe simultaneously through a dichroic beam splitter that divides the wavelength range shortward and longward of $26\,\mu\text{m}$. Alternatively, the long wavelength array can be used by itself as the dichroic is removed from the light path, gaining a sensitivity of ~ 2.5 . We observe the 11.1 and $37.1\,\mu\text{m}$ together (hereafter "mode 1") and the 19.7 and $31.5\,\mu\text{m}$ together (hereafter "mode 2"). We set the 1σ sensitivity threshold to that of a moderately rising SED for a $1.5\,L_\odot$ source, which is scaled appropriately for the distance to the cluster. This is an attempt at probing the same luminosities at all distances and obtain a consistent sample of YSOs.

TABLE II.1: List of desired sensitivities

Distance (pc)	1 σ minimum detectable flux (Jy)				Corresponding minimum L_\odot
	11 μm	19 μm	31 μm	37 μm	
200.0	0.1	0.1	0.32	0.7	~ 0.5
400.0	0.1	0.1	0.32	0.6	~ 1.5
600.0	0.05	0.04	0.18	0.25	~ 1.5
800.0	0.02	0.02	0.1	0.12	~ 1.5
1,000.00	0.01	0.01	0.06	0.1	~ 1.5

List of desired sensitivities for different distances.

However, for the most nearby clusters, the corresponding observing time was so short that the overhead from the observatory was very costly. Hence, we put a lower threshold to the integration time of 30 s. Similarly, the sensitivity of the $37\,\mu\text{m}$ band is such that in order to be consistent with our sensitivity target, this band was heavily driving the observing time using mode 1. Hence, we observe in this mode as long as is required to

meet the sensitivity target for the 11 μm band, and request more observations in the 37 μm band on its own (hereafter "mode 3"). This allows us to request less total observing time while keeping our sensitivity self-consistent. A summary of our target sensitivities for various distances is shown in Table II.1.

Various observing techniques are available to the FORCAST user to deal with background subtraction. The most robust techniques are very costly in terms of overhead for the observatory, so we decided to be audacious and requested the cheapest observing mode: the Chop-Nod-Chop mode (CNC), combined with 9 ditherings for each field, which dramatically helps when co-adding images together. Most of our data was processed by the SOFIA automated pipeline that provided calibrated Level 2 images, except for the data from the first few flights, for which we received the help of one of FORCAST's Principal Investigator, Dr. Joe Adams, who processed the raw data through his own instrument pipeline.

The data were acquired over 10 SOFIA flights spanning multiple years, with the last batch dating from February 2015. The actual observing times for each band and cluster is shown in Table II.3. In that table, we have estimated the time for the 37 μm band using a composite formula that levels the observing time from mode 3 to that of mode 1, considering their respective sensitivities. We obtained about 10 h of on-sky data, and 10 out of our 12 original target clusters were observed.

To complement our observations, we proceed to an archival search to find publicly available WISE, *Spitzer*, and *Herschel* images. Most of our targets have already available *Spitzer* IRAC and/or MIPS photometry (**Megeath:2012cn**; mostly from Gutermuth et al., 2009; Evans et al., 2009), which we use in the relevant cases. In the cases where no IRAC photometry was available, we applied our own photometry algorithms. We could

TABLE II.3: List of targets

Cluster	Coordinates (J2000)	SOFIA Flight IDs	N_{Fields}	d (pc)	T_{11} (s)	T_{19} (s)	T_{31} (s)	T_{37} (s)
Cepheus A	22h56m10s +62d03m26s	F132 F109	2	730	206	234	235	490
Cepheus C	23h05m45s +62d30m05s	F132	1	730	150	121	121	286
IRAS20050	20h07m05s +27d28m51s	F166 F131	2	700	321	224	256	266
NGC1333	03h29m00s +31d17m20s	F129 F193 F190	9	240	530	558	467	446
NGC2071	05h47m06s +00d21m45s	F192	2	420	36	25	33	42
NGC2264	06h41m07s +09d33m35s	F156	4	913	495	300	331	587
NGC7129	21h43m07s +66d06m42s	F109	1	1000	383	214	214	709
Ophiuchus	16h27m05s -24d30m29s	F157	11	150	396	468	501	365
S140	22h19m23s +63d18m44s	F129	1	900	322	393	393	568
S171	00h04m01s +68d34m50s	F132	1	850	253	219	219	476

List of observed targets. For each cluster, we list the SOFIA flights on which the data was taken, the number of individual fields within the cluster, the distance, and the total integration time for each of the 4 observation bands, including all fields. Note that the 37 μm time quote is a composite time calculated by combining the exposure time of mode 1 with that of mode 3, as discussed in the text.

not find published photometry for the targets with available *Herschel* images, hence we also used our own photometry pipeline to derive fluxes. In some cases, we find previously published 1.3 mm continuum measurements to help constrain the long-wavelength behavior of the SEDs.

4 FORCAST characterization

In addition to the raw images, a number of calibrators were observed during each flight for different dichroic settings and wavelength bands. These calibrators are usually bright stars which guarantee to be point sources for SOFIA's angular resolution, and have very predictable mid-IR fluxes, so they can be used both for flux and PSF calibration. We use them for two purposes: the first is to obtain a robust metric to determine whether sources

are extended or not; the second is to determine the aperture correction factor which will later be used for aperture photometry.

4.1 PSF size

The size of the PSF can be defined in multiple ways, we adopt the approach of characterizing the PSF using its encircled energy distribution. Fig II.2 shows the average of the normalized encircled energy distribution of the PSF, measured on all the calibrators of our sample. Each curve represents one of the five different combinations of bandpass filter and dichroic setting that we use for our observations. For each radius, the total energy is the sum of the pixels within the circular aperture of that radius, to which we subtract an estimate of the background in an annulus around the source (see Section II.2 for details on the background subtraction methods).

As expected, the PSF at 37.1 μm is larger than the PSFs at shorter wavelengths, but less than the traditional diffraction limit rule. This indicates that additional PSF smearing is occurring at short wavelengths, likely due to plane jitter and pointing errors, which is consistent with what other authors have found (e.g. Herter et al., 2013). Throughout all the flights, point source calibrators always have the same encircled energy distribution shape within $\sim 4\%$ rms.

To look at the behavior of the PSF in more detail, we can use the half width at half maximum of the encircled energy distribution, R_{50} as a proxy for PSF size. The variation of this quantity for the various flights, bandpass/dichroic setting, and calibrators used is showed in Fig. II.3. This shows the flight-to-flight differences and, for some calibrators, the in-flight variability. We find that the latter is usually small, except for the SOFIA flight on 05-02-2014, for which the spread is quite considerable and could have been caused

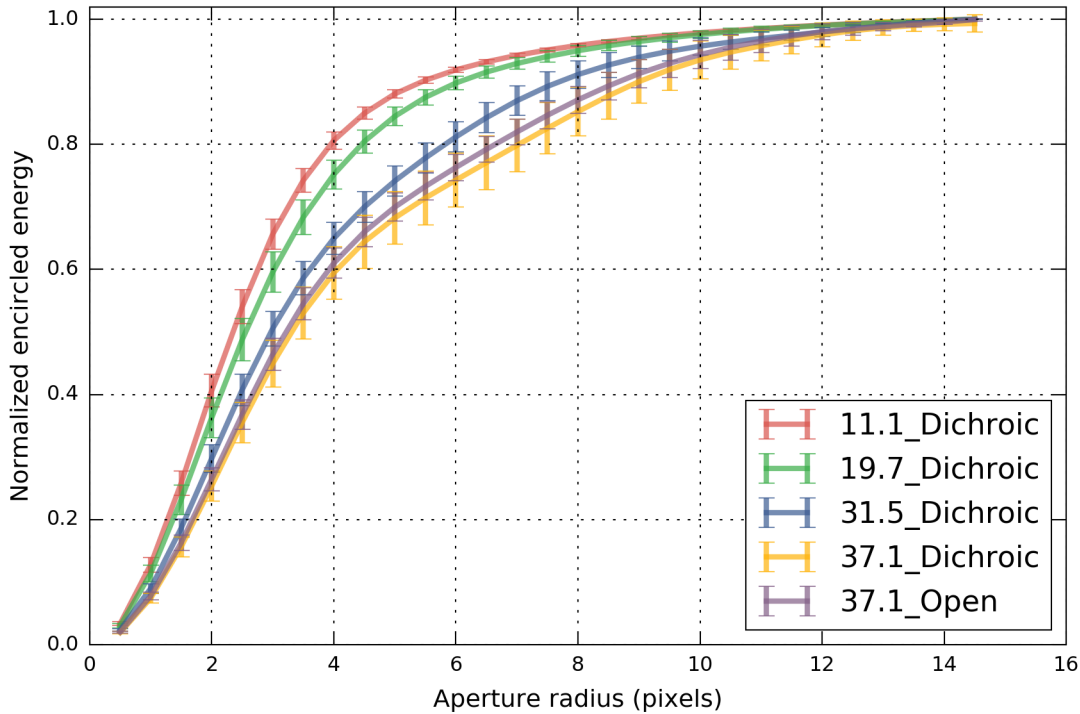


FIGURE II.2: Average PSF encircled energy distribution profile for all calibrator observations.

by instrumental malfunction or abnormal levels of jitter. The variation from flight to flight is larger than the variation within a given flight, which indicates variability in the observing conditions, systematics, or thermal radiation environment of the observatory between different flights. Even considering the flight-to-flight and calibrator-to-calibrator variations, the overall spread in R_{50} for a given observation setting is almost always less than 10%, making this metric a useful reference to compare with scientific data. In our analysis we will compute R_{50} for our sources and compare it to the R_{50} from the current flight for the same filter setting, if the calibration file exists. If no calibration file exists for a given setting, we use the mean R_{50} for that setting from calibrators observations in other flights. The ratio $R\%$ of these two quantities helps quantify the extension of the source, to within $\sim 10\%$.

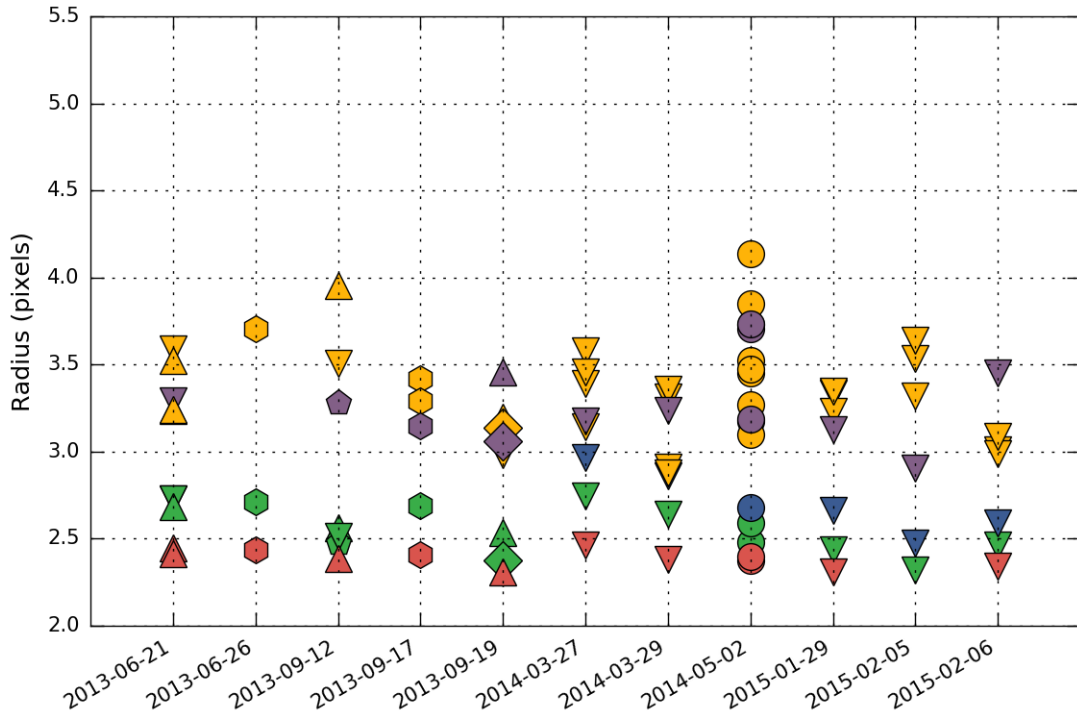


FIGURE II.3: Distribution of R_{50} for all calibrators observations within each bandpass. In red: 11 μm band, with dichroic; in green: 19 μm band, with dichroic; in blue: 31 μm band, with dichroic; in yellow: 37 μm band, with dichroic. Down triangles: α Boo; Pentagons: α Cet; Diamonds: α Tau; Up triangles: β And; Hexagons: β Peg; Circles: β UMi;

4.2 Aperture correction factor

In Fig. II.2, we observe that the encircled energy does not vary much by the time the aperture reaches a radius of 12 pixels, so we consider this fiducial aperture as our "total flux" aperture. The goal of aperture photometry is to estimate the amount of flux in this large aperture, which we consider to be the total amount of flux from the source, by only measuring flux within a much smaller aperture. This has the advantage of reducing contamination from other sources, and increases the signal-to-noise ratio of the flux estimate since the pixels near the tail of the PSF usually contain more noise than signal. In Fig II.5, we plot the aperture correction factor that we compute from the ratio of the flux measured

within an aperture of 3 pixels radius and this 12-pixel aperture. Not surprisingly, this graph follows very closely the plot of R_{50} from Fig II.3, showing the close link between the aperture correction factor and the shape of the calibrator's PSF. We match each observation in our data to the mean of the aperture correction factors for the same observation setting and flight.

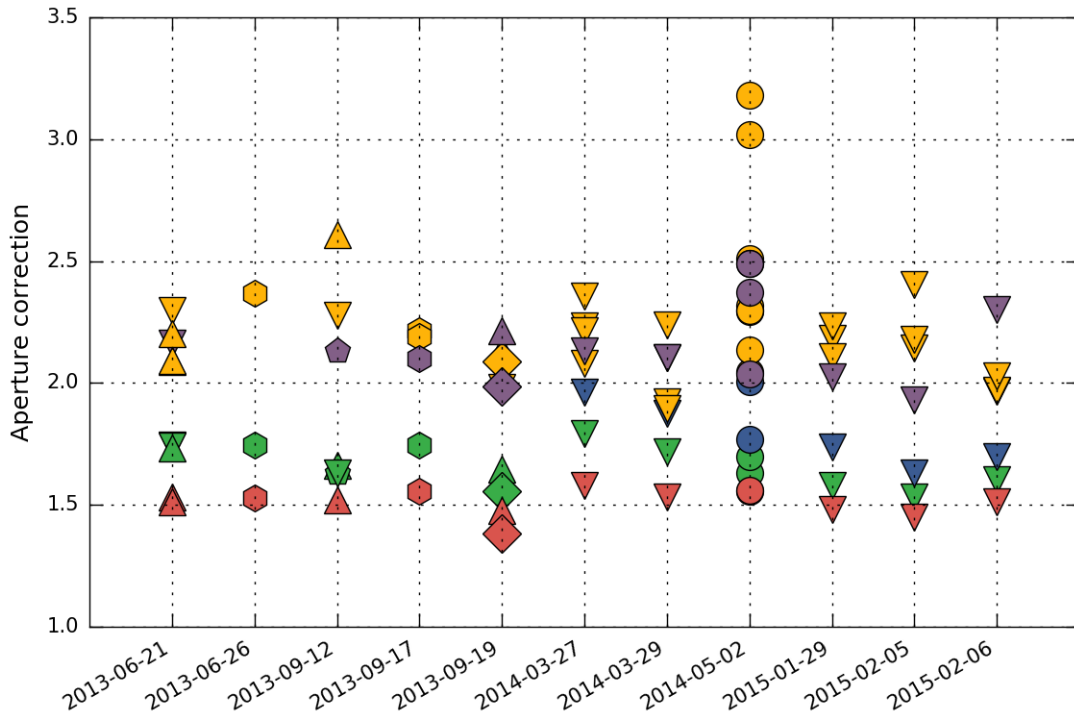


FIGURE II.4: Instrumental response and aperture correction

4.3 Instrument response and overall uncertainty

To validate our approach, we take a look at the calibrator fluxes after normalization by the calibration factor, which is provided directly by the FORCAST pipeline. This calibration factors converts the pixel digital value a physical flux density unit, and presumably is determined using the flux from calibrator stars as well. Here we re-measure the flux from each calibrator for each observation setting and each flight, using our standard aperture

photometry method and background subtraction. Ideally, we would always obtain the same flux for each setting and calibrator, independently of the flight, an assertion we find true to within $\sim 5\%$. The in-flight errors are typically lower than this. This validates our aperture photometry method, and we can trust that the instrument's systematics are well-behaved to within these levels.

This would suggest that we can adopt systematic 1σ uncertainties of $\sim 5\%$, a value which is consistent with the published uncertainties of $3\sigma \approx 20\%$ (**DeBuizer:2012ie**).

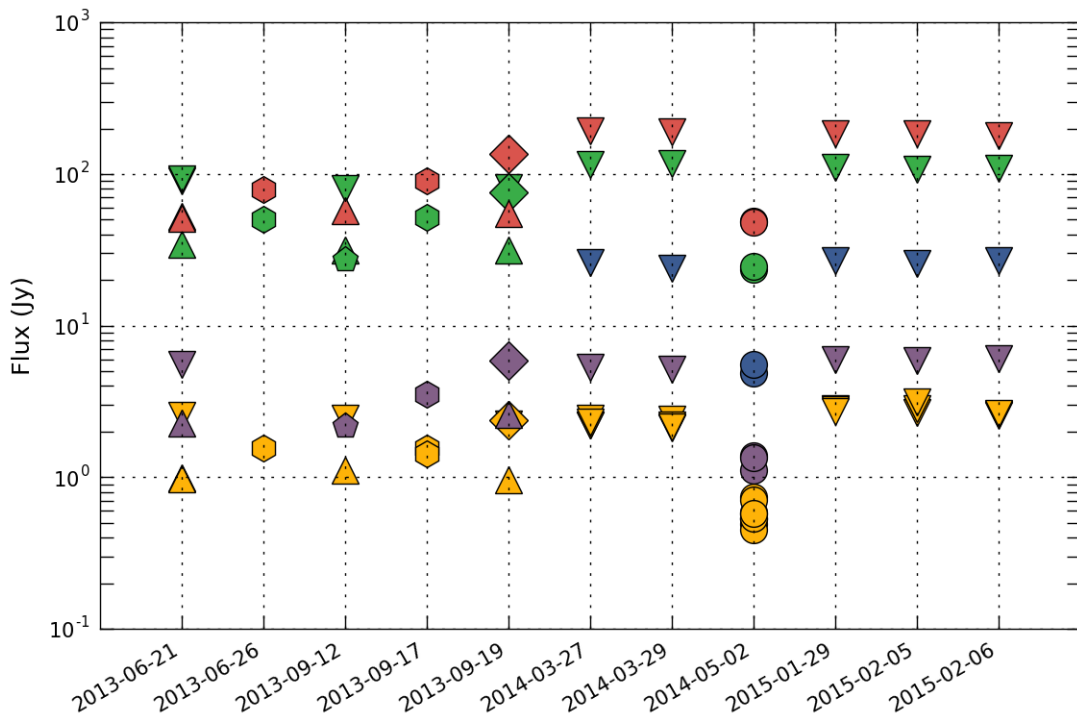


FIGURE II.5: Instrumental response

5 Data reduction and photometry

The data are processed through various versions of the online pipeline to yield Level 2 data products available on the archive (Herter et al., 2013). We apply our own reduction procedure and photometry pipeline on those products to derive final images, source positions, fluxes and sensitivities. Our software makes extensive use of the Python *astropy* package (Astropy Collaboration et al., 2013) and its associated modules *photutils* and *APLpy*.

5.1 Pre-treatment

Some manual treatment of each image is necessary before it can be analyzed by our software, which follows this procedure: a) visually aligning the WCS coordinate system, often 10-20" off, using point sources and archival data from other wavelengths and facilities such as IRAC 8 μm ; b) cropping the images to clean off the nodded fields, and c) identify the coordinates of each source, both point-like and extended.

After these manual steps, the Level 2 images are multiplied by the calibration factor provided by the online pipeline, which converts them to Jy/pixel. We do not proceed to any systematic color correction, but the effects on the fluxes are very small (Herter et al., 2013).

1. Adjust WCS coordinates: use images at other wavelengths (2MASS, IRAC, MIPS, WISE) to re-align the (RA, DEC) position of the field. We estimate that this process is good to within one SOFIA pixel (0.768") for the fields where one or more point sources can be identified. Extended fields are less trustworthy, since matching the extended emission to other wavelengths is harder. The rotation of the field produced by the SOFIA pipeline is correct for all of our data.

2. Crop each image, remove chopped fields, remove artifacts.
3. Identify and categorize sources: isolated point sources, clustered point sources, and extended sources. For extended sources, a circular or elliptical aperture is used to try to encompass the entirety of the emission.
4. Manually identify a location in the field that corresponds to a representative background.

5.2 Source flux extraction

We feed the adjusted FITS and associated metadata files to our photometry pipeline. For each identified source, we determine its flux in all bands using aperture photometry with local background subtraction. The aperture correction factor we use is the one determined from the calibrators observed for the same observation setting during the same flight as the one when the data was taken. If a calibrator is not available during the flight, we use the average aperture correction factor taken over 9 of our 10 flights (we choose to exclude the flight on 05/02/2014 which seems to have abnormal behavior).

We distinguish between 3 types of sources after manual identification: *isolated*, which are point sources with no nearby objects; *clustered*, which are point sources with nearby objects; and *extended*, which are not consistent with being point sources.

For point sources that are isolated, we use our standard aperture of 3 pixels at all wavelengths. We consider an annulus surrounding the source extending from 12 to 20 pixels radius (24 to 40 for clustered sources): the local background is determined from the mode of the pixels in the annulus, while the sensitivity is calculated by measuring

the standard deviation of the flux values within 4-pixel apertures spread over that annulus (**Shimizu:2016if**). We apply the aperture correction derived from the calibrator observations taken during that flight.

For extended sources, an elliptical aperture is determined manually from the 37 μm images. The local background is determined from the mode of an elliptical annulus, with an inner boundary at the elliptical aperture and an outer boundary corresponding to an ellipse 20% larger. The sensitivity quoted is the point source sensitivity, and is determined following the same method as for point sources, using the standard deviation of apertures spread across the elliptical annulus.

The photometry from sources that were observed in different flights is then combined to increase the signal-to-noise ratio. This combination takes into account the sensitivity of each source by appropriately weighing each image.

The source sensitivity calculated is added to the systematic uncertainty of the instrument, for which we follow the recommendation from (Herter et al., 2012) to adopt a 7%, 1σ uncertainty.

To validate our flux extraction method, we compare our results with data from **Harvey:2012kw** who observed one of the sources in our sample, S140. Their photometry (shown in their Table 1) of IRS 1, 2 and 3 (respectively corresponding to our targets S140.5, S140.4, and S140.3) is compared to our photometry in Table II.5. We find very good agreement between our fluxes and theirs. The remaining differences can always be explained by slight differences in the center location of the aperture.

TABLE II.5: SOFIA photometry comparison

SOFIA name	F11	F11L	F19	F31	F31L	F37	F37L
	Jy	Jy	Jy	Jy	Jy	Jy	Jy
S140.3	10.28	9.70	101.49	419.41	401.00	525.90	669.00
S140.4	3.80	4.00	88.95	337.22	368.00	352.07	485.00
S140.5	110.57	110.00	830.97	2065.13	1585.00	2278.61	2176.00
Sum of sources in cluster	124.65	123.70	1021.40	2821.76	2354.00	3156.58	3330.00
Total cluster emission	135.20	145.00	1194.57	4449.46	3780.00	5840.64	6730.00
Ratio	1.08	1.17	1.17	1.58	1.61	1.85	2.02

Comparison of SOFIA four-band photometry from **Harvey:2012kw** on S140 (columns with 'L'). All fluxes are in Janskies. The authors' "total emission" actually represents the total emission in the entire field of view, whereas our measurement corresponds to a manually-selected source region encompassing only the dense core. The total emission in the entire field of view is less representative, as it could include contribution from other sources as well as areas of negative flux from the chopping and nodding steps. In this cluster, there is a large amount of emission which is not due to the three identified sources.

TABLE II.7: FORCAST Sensitivities

Cluster	F11			F19			F31			F37			Sources
	σ^{man}	σ^{std}	σ^{th}										
CepA	0.07	0.04	0.05	0.11	0.05	0.05	0.19	0.07	0.16	0.26	0.09	0.34	4
CepC	0.03	0.03	0.04	0.10	0.05	0.04	0.19	0.06	0.16	0.16	0.09	0.30	4
IRAS20050	0.04	0.03	0.04	0.08	0.04	0.05	0.13	0.05	0.16	0.30	0.11	0.32	7
NGC1333	0.12	0.04	0.07	0.07	0.07	0.07	0.22	0.08	0.25	0.48	0.13	0.52	11
NGC2071	0.19	0.10	0.12	0.32	0.15	0.15	0.21	0.22	0.49	0.45	0.28	0.81	6
NGC2264	0.07	0.03	0.05	0.19	0.05	0.06	0.28	0.07	0.20	0.21	0.09	0.43	21
NGC7129	0.07	0.03	0.03	0.10	0.04	0.03	0.26	0.09	0.12	0.17	0.08	0.19	5
Ophiuchus	0.11	0.05	0.08	0.16	0.07	0.08	0.31	0.09	0.27	0.41	0.18	0.65	19
S140	0.04	0.03	0.03	0.16	0.03	0.03	0.21	0.07	0.09	0.35	0.11	0.21	7
S171	0.04	0.03	0.03	0.07	0.04	0.03	0.07	0.05	0.12	0.16	0.06	0.23	2

For each band, we measure the 1σ sensitivity σ^{man} and σ^{std} in each field from the data using two different methods (see text), and present here the median of all fields. The theoretical sensitivity σ^{th} corresponds to the expected sensitivity for the actual integration time, using the SOFIA FORCAST observation planning tools and assuming moderate water vapor content. All sensitivity values are in Janskies.

5.3 Image sensitivity

In order to determine the absolute sensitivity in the image, we use two methods. First, we manually determine a region in each cluster that visually appears devoid of flux. We calculate the sensitivity as if this background region was a source, by patching apertures in an annulus around this background location and calculating the standard deviation of the obtained fluxes. We call this sensitivity measurement σ^{man} . The main downside of this method is that it requires a manual operation to select the appropriate background field, and hence could have more variation depending on which field we select. Second, we use a routine that iteratively isolates the pixel values above 2σ of the image, in order to remove the contamination from our actual sources. The standard deviation of the resulting image is then calculated, and is multiplied by the square root of the number of pixels in an aperture of 3 pixel radius. This corresponds to a floor sensitivity σ^{std} . We present our results in Table II.7, where we also compare this sensitivity with the expected sensitivity σ^{th} obtained using the online calculator with the actual exposure time of our images. We note that usually, the theoretical values are more in agreement with our first method.

5.4 Other photometry

While SOFIA provides mid-IR photometry, we looked in the literature for published fluxes on our targets in order to reconstruct more complete SEDs. In addition to our four SOFIA bands, our table includes data from 2MASS, *Spitzer*, and other instruments. Photometry from these sources is published in online catalogs, which we programmatically cross-reference with the positions of our targets. The closest target that corresponds to a Vizier location query is selected to be the correct catalog match. For the 2MASS data, the location of the target needs to be less than $2''$ away from our coordinates for point sources,

and $5''$ for extended sources. For the *Spitzer* data, the matching radius is $3''$ for point sources and $10''$ for extended sources. In addition to automated online catalog searches, we also add values for sources in NGC2071 from Kempen et al. (2012).

For our two most clustered cases in the cores of NGC2071 and IRAS20050+2720, the published catalogs do not have all available fluxes. We assume that the sources are so clustered that they the source extraction software from these authors do not register them as point sources, due to confusion or saturation effects. Hence we adapt our own photometry routines for these clustered environments and obtain the fluxes directly from the calibrated Level 3 images themselves, which are all available on the archive. In Table II.9, we compare our photometry results with published fluxes from **Megeath:2012cn** and Gutermuth et al. (2009) for isolated sources elsewhere in these same fields of view. We use the *Spitzer* handbook recommendations for aperture photometry on *Spitzer* archival images ($2.4''$ aperture with and an annulus that extends from 12 to $20''$). We find that our results are within 10% of these other authors' results, which can reflect a simple difference in exact aperture centroiding position.

In some cases, we also found archival Herschel images, although no published photometry was available for most our sources. We then apply our same aperture photometry routines for those calibrated Herschel images, using aperture and background subtraction parameters from (**Shimizu:2016if**) for the PACS and SPIRE. We find also very good agreement between our photometry results for the PACS $70\,\mu\text{m}$ band and the published *Spitzer* MIPS $70\,\mu\text{m}$ for some of these sources.

TABLE II.9: Spitzer photometry comparison

SOFIA name	i1	i2	i3	i4
	Jy	Jy	Jy	Jy
NGC2071.1	0.060	0.056	0.004	-0.021
NGC2071.3	0.018	-0.010	-0.004	-0.047
NGC2071.4	0.090	-0.054	0.036	-0.066
NGC2071.5	-0.130	-0.109	-0.144	-0.139
IRAS20050.1	0.020	0.039	0.017	0.131
IRAS20050.3	0.181	0.122	0.082	0.121
IRAS20050.6	-0.044	-0.046	-0.092	-0.056

Note: Fractional difference between our own aperture photometry on *Spitzer* archival images and published *Spitzer* photometry from [Megeath:2012cn](#) for NGC2071, and Gutermuth et al. (2009) for IRAS20050+2720. When values are negative, it means that their photometry is lower than ours.

6 Data products

6.1 Mosaics

The SOFIA FORCAST archival images consist of ~ 200 individual images, each representing a field at a given wavelength. Some fields are revisited multiple times when the entire observation could not happen in a single flight leg. These individual fields are processed and mosaiced together to form one single map for each wavelength and each cluster.

Before mosaicing the fields, we proceed to a 2D background subtraction. This method divides the images into sections of 50×50 pixels, estimates the median in each cell, and fits a 2D function to these median values. This function is then used to construct a smooth background, which is then completely removed from the image. Each background-subtracted image is then calibrated (using the calibration factor that is supplied by the FORCAST pipeline), and weighed by its exposure time before it is co-added into a mosaic in the WCS coordinate frame. Note that although these maps are useful to take a quick

glance at the flux distribution and spot artifacts, the actual photometry described in the previous sections uses each individual raw field, before the mosaicing and without background subtraction. If a source is present in multiple fields, the photometry from each of these fields is combined to provide a better flux estimate.

In Fig. II.6 we present a variety of maps from our cluster sample. Each map is a three-color image (red: 37 μm , green: 31 μm and blue: 19 μm), and the scale and stretch of each color is adjusted to balance each color.

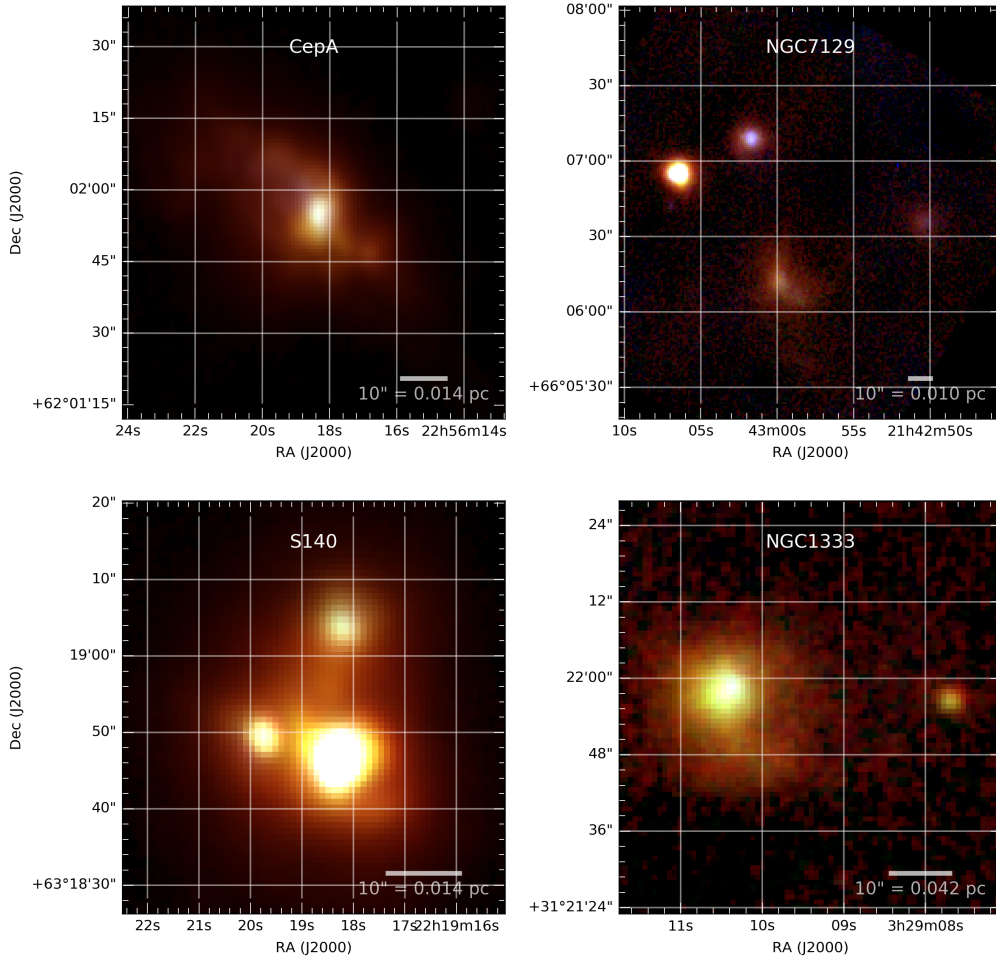


FIGURE II.6: Selected sample of sources

6.2 Photometry and SEDs

The main type of data made available to the community is a list consolidated list of fluxes for most of our clusters, where we gather 2MASS, *Spitzer*, FORCAST, *Herschel*, SCUBA, and SMA data, when available, for ~ 90 sources. Most sources are point sources for the SOFIA FORCAST 37 μm band, but some sources present a certain spatial extension which was not known before.

A few other parameters are determined from the FORCAST data and shown in the data release: the R_{37} , which consists of the ratio of R_{50} for the source and R_{50} for the last observed calibrator; the spectral index and its uncertainty, computed out of the fluxes from 2.2 μm to 37 μm ; and the bolometric luminosity and temperatures for each source. An excerpt of the final table is shown in Table II.11.

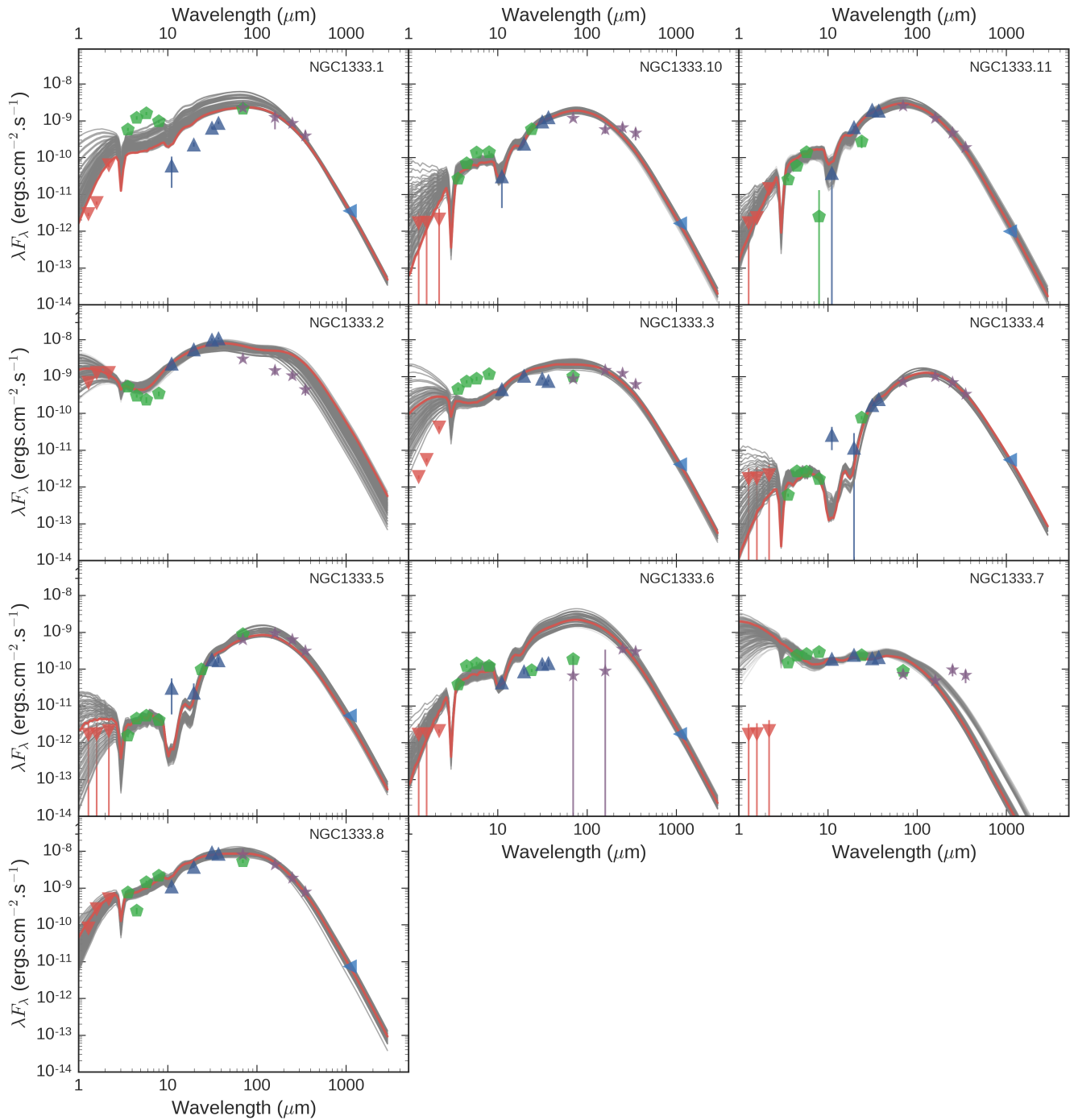


FIGURE II.7: SEDs of the point sources in NGC1333. The red curve represents the best fit. The grey curves represent all the fits with R within 0.5 of the best fit. Red triangles: 2MASS. Green diamonds: *Spitzer* (our data or data from other existing catalogs). Dark blue triangles: FORCAST (our data). Purple stars: *Herschel* (our photometry). Green triangles: Data from (vanKempen:2009ku) and (Kempen et al., 2012). Light blue triangles: Data from Enoch:2009ch

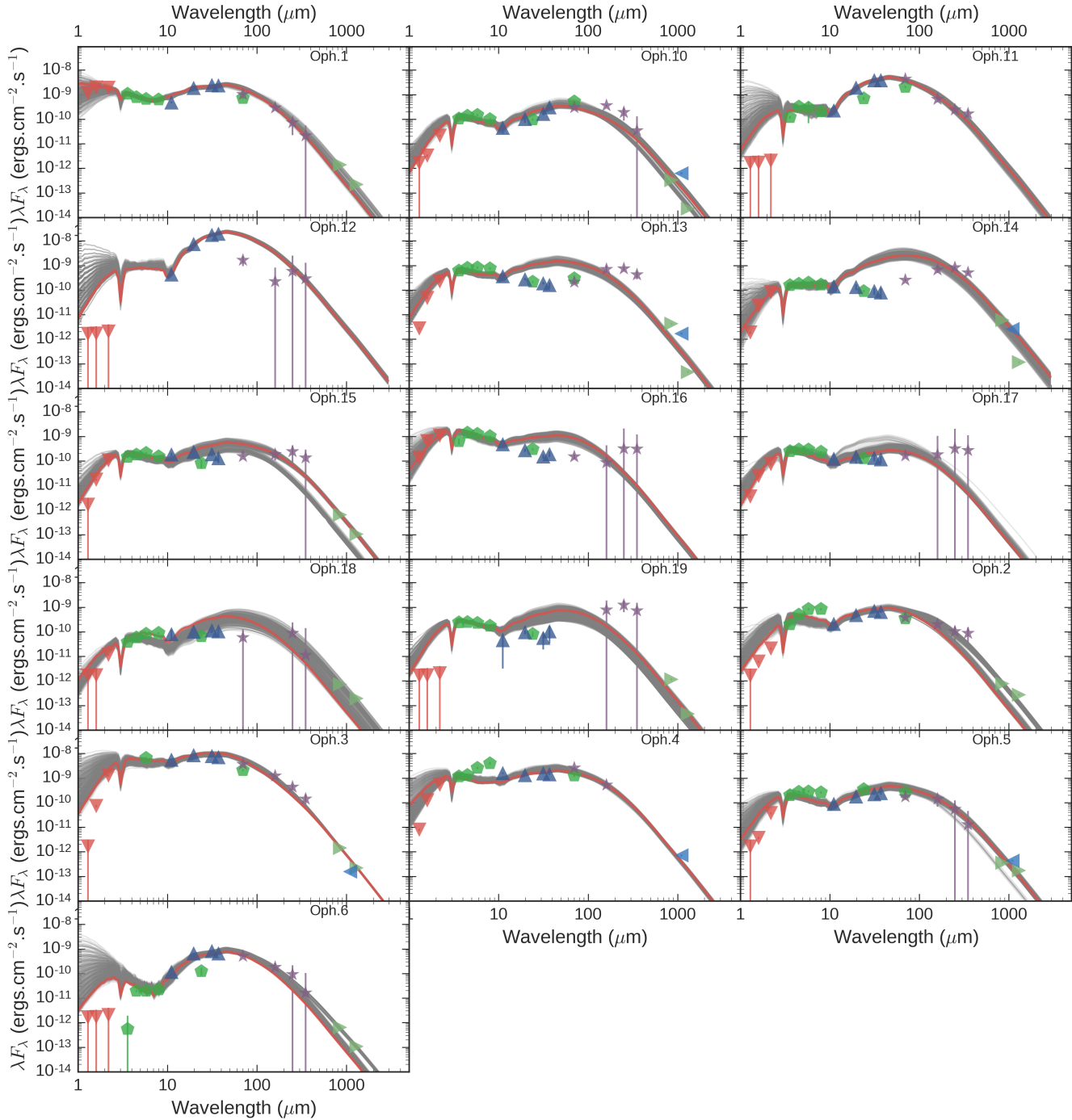


FIGURE II.8: SEDs of the point sources in the Ophiuchus cluster. Same legend as Fig. II.7

TABLE II.11: Extract of NGC1333 photometry.

SOFIA name	Coordinates	R37	Lbol	Tbol	j	e_j	h	e_h	ks	e_ks	i1	e_i1	i2	e_i2
NGC1333.1	03h29m07.7s +31d21m57.0s	0.746	8.385	22.401	0.0012	0.0001	0.0031	0.0003	0.0450	0.004	0.696	0.070	1.800	0.180
NGC1333.2	03h29m10.3s +31d21m55.5s	2.232	27.832	24.356	0.2853	0.0285	0.6539	0.0654	0.9010	0.090	0.637	0.064	0.446	0.045
NGC1333.3	03h29m01.5s +31d20m20.5s	0.904	8.104	20.630	0.0008	0.0001	0.0029	0.0003	0.0296	0.003	0.544	0.054	1.090	0.109
NGC1333.4	03h29m11.1s +31d18m30.8s	1.103	3.056	4.204	0.0007	0.0007	0.0009	0.0009	0.0015	0.002	0.001	0.000	0.004	0.000
NGC1333.5	03h29m10.6s +31d18m19.6s	1.623	2.786	4.424	0.0007	0.0007	0.0009	0.0009	0.0015	0.002	0.002	0.000	0.007	0.001
NGC1333.6	03h29m13.0s +31d18m13.8s	0.951	1.155	17.248	0.0007	0.0007	0.0009	0.0009	0.0015	0.000	0.046	0.005	0.180	0.018
		i3	e_i3	i4	e_i4	F11	e_F11	F19	e_F19	m1	e_m1	F31	e_F31	F37
NGC1333.1	03h29m07.7s +31d21m57.0s	3.060	0.306	2.550	0.255	0.225	0.169	1.502	0.208	–	0.260	6.886	0.640	10.994
NGC1333.2	03h29m10.3s +31d21m55.5s	0.448	0.080	0.913	0.128	8.414	0.596	36.517	2.562	–	–	106.490	7.457	135.723
NGC1333.3	03h29m01.5s +31d20m20.5s	1.690	0.211	3.060	0.306	1.681	0.131	6.902	0.493	–	0.069	9.256	0.656	9.406
NGC1333.4	03h29m11.1s +31d18m30.8s	0.005	0.001	0.004	0.000	0.097	0.060	0.076	0.115	0.607	0.061	1.785	0.209	3.040
NGC1333.5	03h29m10.6s +31d18m19.6s	0.010	0.001	0.011	0.001	0.114	0.093	0.150	0.119	0.771	0.077	1.946	0.234	2.166
NGC1333.6	03h29m13.0s +31d18m13.8s	0.274	0.027	0.320	0.032	0.160	0.035	0.570	0.093	0.735	0.074	1.446	0.180	1.806
		e_F37	m2	e_m2	H70	e_H70	H160	e_H160	H70	e_H70	H160	e_H160	H250	e_H250
NGC1333.1	03h29m07.7s +31d21m57.0s	0.948	49.300	4.930	52.724	5.272	66.529	35.197	52.724	5.272	66.529	35.197	71.541	14.258
NGC1333.2	03h29m10.3s +31d21m55.5s	9.507	–	–	70.039	7.004	77.574	20.036	70.039	7.004	77.574	20.036	87.661	15.014
NGC1333.3	03h29m01.5s +31d20m20.5s	0.695	23.400	2.340	20.218	2.022	78.316	7.832	20.218	2.022	78.316	7.832	101.472	18.943
NGC1333.4	03h29m11.1s +31d18m30.8s	0.341	–	–	16.609	1.661	53.689	5.369	16.609	1.661	53.689	5.369	57.215	6.293
NGC1333.5	03h29m10.6s +31d18m19.6s	0.377	20.600	2.060	14.627	1.463	49.868	4.987	14.627	1.463	49.868	4.987	52.536	6.166
NGC1333.6	03h29m13.0s +31d18m13.8s	0.345	4.290	0.429	1.527	3.883	4.702	13.332	1.527	3.883	4.702	13.332	29.105	6.272
		H350	e_H350	H500	e_H500	S850	e_S850	F1100	e_F1100	S1300	e_S1300	α	e_α	
NGC1333.1	03h29m07.7s +31d21m57.0s	45.559	17.857	24.264	16.301	–	–	1.300	0.130	–	–	0.280	0.564	
NGC1333.2	03h29m10.3s +31d21m55.5s	51.506	16.114	24.742	13.062	–	–	–	–	–	–	1.243	0.000	
NGC1333.3	03h29m01.5s +31d20m20.5s	70.907	17.371	40.867	11.474	–	–	1.500	0.150	–	–	0.714	0.385	
NGC1333.4	03h29m11.1s +31d18m30.8s	38.449	6.033	18.594	4.666	–	–	2.000	0.200	–	–	1.864	0.458	
NGC1333.5	03h29m10.6s +31d18m19.6s	36.232	6.189	18.007	4.878	–	–	2.000	0.200	–	–	1.705	0.273	
NGC1333.6	03h29m13.0s +31d18m13.8s	34.781	8.007	21.255	6.628	–	–	0.630	0.063	–	–	1.001	0.501	

Note: The complete version of this table is made available electronically

6.3 Fitted physical parameters

The spectral index distribution for the point sources in our sample, using a modified spectral index extending out to 37 μm, is shown on the left of Fig. ???. Most sources have positive spectra index, indicative of a rise in the SED and a large proportion of long-wavelength emission. These objects are more dusty, and believed to be younger than objects with negative spectral index. A closer inspection reveals that targets with negative index mostly lie in the Ophiuchus cluster, and can consist in late type I objects which have already cleared most of their envelopes. These exhibit higher bolometric temperatures, as most of the emission is shifted towards shorter wavelengths.

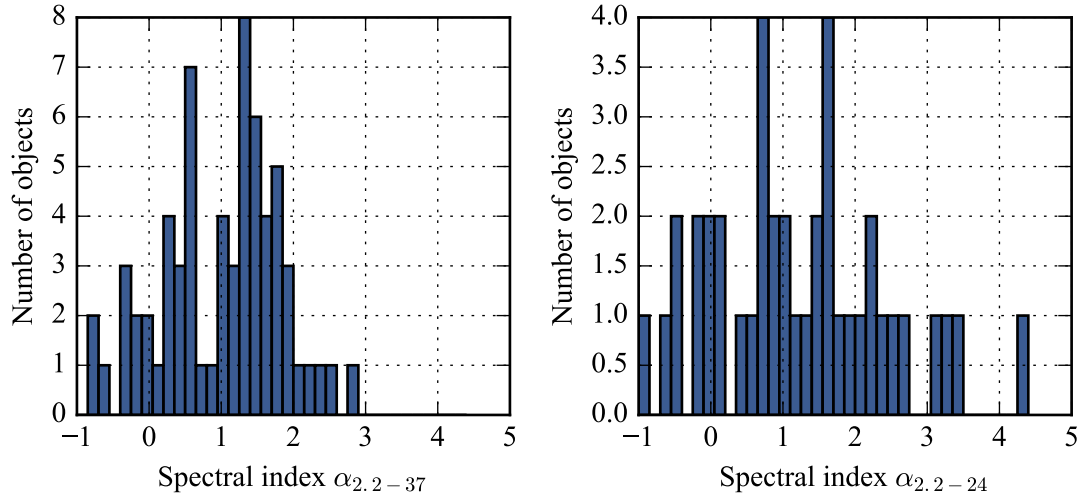


FIGURE II.9: Spectral Index distribution of point sources. *Left:* standard determination of the spectral index, using 2MASS and *Spitzer* from 2 μm to 24 μm, when data is available. *Right:* Determination of the spectral index using data from 2MASS, *Spitzer* and our FORCAST data up to 37 μm. The distribution changes significantly when you account for the longer fluxes in these clustered regions.

The final data release also includes all of the physical parameters derived using the technique from Section ??, as well as their uncertainties.

7 SED fitting

7.1 A custom grid of models

SED fitting is prone to many degeneracies: usually many geometrical and physical parameters are used to construct detailed radiative transfer models, but only a handful of measurement points are available to fit, leading to a dramatically under-constrained problem. As our starting point of our investigation of the SEDs of these sources, we used the *sedfitter* tool from (Robitaille et al., 2006). These authors computed a large grid of tens of thousands of SED models using a radiative transfer code by (Whitney et al., 2003a), by varying 14 geometrical and physical parameters in the dust density grid such as the size of the disk, the accretion rates, the radius and mass of the envelope, etc. The models are then evaluated in the bands corresponding to our data, and a χ^2 metric is evaluated for each model. By exploring the distribution of χ^2 , we noticed, as expected, the very large correlations between the parameters which is indicative of many local minimas in the grid. Hence, inferring geometrical and physical parameters from such a grid can be misleading.

We used a more modern version of the same core radiative transfer code, called Hyperion, to develop our own capability of simulating SEDs and understand the sensitivity of these parameters on the SED shape of our Class 0 and I sources. Based on our investigation, the degeneracy between viewing angle and multiple geometrical parameters is considerable. In particular, the sensitivity of the disk properties is minimal, as most of the SED properties are determined almost entirely by the envelope. In addition, parameters of the central source such as the mass, radius and temperature are irrelevant, as they are all combined into one single term, which is the central luminosity. Similarly, the luminosity created when simulating a disk accreting onto the central object can not be distinguished

from a more luminous central object and a non-accreting disk. Finally, we find that there is very little difference between Ulrich envelope models and standard power-law envelopes (see for example Fig. 14 from Whitney et al. (2013)), except that the latter can more directly be related to physical parameters such as the envelope mass.

From these findings, we created a simplified grid of models by significantly reducing the number of parameters. The resulting choices are presented in Table II.13. Unlike most authors, who use multiple kinds of dust models for different regions of the SED (which add complexity and number of parameters), we simply use the same dust model (OH5) for both the envelope and the disk, and assume a 1:100 dust-to-gas ratio. The two main parameters that we use are the central luminosity and the envelope mass, as these are the two main physical quantities that we are trying to determine from the data.

We constructed a wrapper program that can run the Hyperion software for the parameters in this grid. Because of time and resource limitations, a moderate number of photons was chosen. The details of our modeling parameters, which will be familiar to the Hyperion user, are described in Table II.15. Note that models of more than $1 M_{\odot}$ are actually run with 1×10^6 photons for imaging, in order to obtain acceptable SNR at short wavelengths.

The grid is composed of 330 models which are modeled with Hyperion. For models of more than $0.5 M_{\odot}$, we interpolate the grid in mass by increments of 20%, which allows for a finer sampling at higher masses, but increases the number of individual models to 914. Each model is sampled at 20 inclinations, 15 values for external extinction, and five different scaling factors, for a total of ~ 1.4 million grid models. Each model is evaluated at all relevant observing bands, from the 2MASS bands all the way to 1.3 mm SMA bands. Given the sparsity of the grid, and the relatively simple model used, we do not apply color

TABLE II.13: SED model grid.

Parameter	Description	Values	Units
Constant parameters			
Central source			
M_*	Stellar mass	1	M_\odot
T_*	Stellar temperature	4000	K
Disk			
Type	Flared or alpha disk	Flared	
M_{disk}	Disk mass	0.01	M_\odot
R_{disk}^{\max}	Disk outer radius	100	au
R_{disk}^{\min}	Disk inner radius	sublimation radius	au
β	Flaring parameter	1.25	
p	Disk surface density exponent	-1	
r_0	Reference distance for scale height	R_{disk}^{\min}	au
h_0	Disk scale height at r_0	$0.01R_{\text{disk}}^{\min}$	au
d	Dust	OH5	
Envelope			
Type	Power-law or Ulrich	Power-law	
R_{env}^{\min}	Envelope inner radius	R_{disk}^{\min}	au
R_{env}^{\max}	Envelope outer radius	5000	au
α	Power	-1.5	
r_0^{env}	Reference radius	R_{env}^{\min}	au
d	Dust	OH5	
Cavity			
r_0^{cav}	Cavity outer radius	R_{env}^{\max}	au
θ_0	Opening angle at r_0^{cav}	10	degrees
	Flaring exponent	1.5	
ρ_0	Density at r_0^{cav}	0	g cm^{-3}
α_e	Density profile exponent	0	
Changing parameters			
i	Inclination angle	0 to 90 in 20 constant increments of $\cos(i)$	degrees
L_*	Central luminosity	5×1.5^p for $p = -4, -3, \dots, 15$ (from 0.99 to 288)	L_\odot
M_{env}	Envelope mass	0.01×1.5^p for $p = -2, -1, \dots, 20$ (from 0.004 to 22.17)	M_\odot
A_V	External extinction	0, 1, ..., 15	
s	Scaling	0.7, 0.85, 1, 1.5, 1.3	

TABLE II.15: Hyperion simulation parameters.

Number of photons (initial)	2×10^5
Number of photons (imaging)	2×10^5
Number of photons (raytracing sources)	1×10^6
Number of photons (raytracing dust)	1×10^6
Lucy max iterations	6
Max photon interactions	1×10^5
Geometrical grid parameters (radial, theta and azimuthal)	400, 199, 2
MRW	True

correction to the fluxes, nor do we convolve the model fluxes with the band transmission function: the resulting corrections usually fall well within our approximations, and do affect significantly the outcome of the fitting.

The scaling factor is used to show the uncertainty in the distance determination (Robitaille et al., 2006), but it can also be considered as a factor to sample different luminosities (**Furlan:2016df**). Indeed, **Furlan:2016df** show that, to first order, changing luminosities by a small amount is approximately equivalent to scaling the SED in flux. In their grid, they use a scaling factor that ranges from 0.5 to 2.0, which allows them to have factors of two between their luminosity steps. We choose a more conservative approach by actually running the grid at closer luminosity steps (factor of 1.5) and hence have a smaller scaling factor.

The extinction parameter is used to represent extinction by material along the line of sight that is *outside* of the core, commonly used for foreground material. A discussion of this parameter is proposed in the following sections.

7.2 Fitting method

In order to determine which model fits the data best, we adopt a metric defined by

Fischer:2012dj

$$R = \frac{1}{N} \sum_i w_i |\log[F_{\text{obs}}(\lambda_i)] - \log[F_{\text{mod}}(\lambda_i)]|, \quad (\text{II.1})$$

where i are the indices of the valid data points, the weights w_i correspond to the inverse of the fractional uncertainty of each measurement, F_{obs} and F_{mod} are the observed and model fluxes respectively, and N is the number of valid measurements. For our models, we set the fractional uncertainty to a minimum of 10%, to avoid having just a few points completely over-constrain the problem.

Furlan:2016df discuss in more detail the meaning of this metric, which differs from a standard χ^2 metric such as the one used by Robitaille et al. (2007). Here R represents a weighted average of the logarithmic deviations between the observations and the model. It is important to note that, although it is normalized, it does not have a statistical interpretation like the standard χ^2 metric does.

For each source, we calculate R for each model in our grid. The model with the smallest value for R is the best-fitting model by this metric, but given our sparse sampling and the errors of our observations, this is not necessarily the best estimate for the model which best fit the data. We can consider two extremes to this case: in the first, the best fit has a value of R which is much lower than for other models. Then, it is clearly the best fit. In the second case, let's suppose that the 1000 best-fitting models lie very close to the best R . In this case, concluding that the model that best fits our observations (and from which will interpret physical quantities) is the one with the minimum R is too strict and

does not account for the uncertainties that are present in this exercise.

In practice, all of our models fall in that second case, since our parameter grid sampling is sufficiently dense. After visual inspection we estimate there is very little significant difference between values of R which are separated by ~ 0.5 , as they all can be considered equally good fits. Hence, for a robust measure of the best-fitting model parameters, we choose the mode (the most likely value) of the parameters from models which are within R_{\min} and $R_{\min} + 0.2$. The error on the parameter estimate is then estimated using the models within R_{\min} and $R_{\min} + 0.5$, and is described in the next section.

7.3 Overview of derived parameters

The distribution of the best fit of the envelope mass and central luminosity is shown in Fig. ???. Our sample covers a broad range of masses, but is naturally biased towards high luminosities given our instrumental sensitivity and cluster selection.

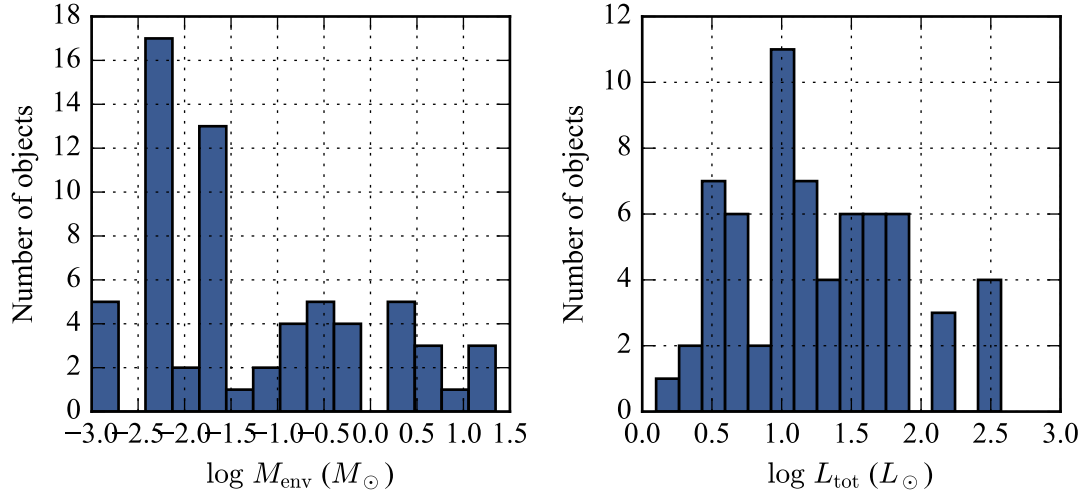


FIGURE II.10: Fitted envelope mass and luminosity distribution.

The simple grid that we used manages to fit most of the data pretty well. The distribution of R for all the isolated point sources is shown in Fig. ???. Note that targets where less data points are available, or where data points are more noisy, usually have lower R than targets with a lot of available data points, even if the fits are not necessarily as good. This has also been observed by (**Furlan:2016df**).

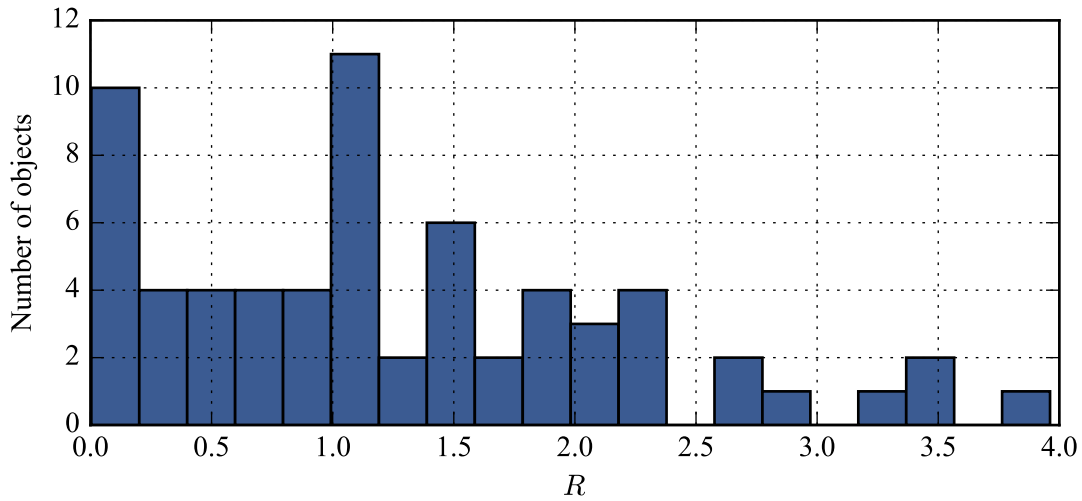


FIGURE II.11: R distribution across all point sources.

For our sample, we can compare the fitted central luminosity, L_{tot} , with the integrated luminosity from the datapoints, L_{bol} (Fig. ??) for our entire sample of point sources. This shows relatively good agreement, although a systematic excess in fitted central luminosity can be observed, which we attribute to the widespread choice of using an external extinction coefficient. By using this external extinction as a model parameter, we artificially reduce the emission at short wavelengths, which would tend to decrease the bolometric luminosity.

The luminosity excess is more pronounced for lower masses, as the short wavelength emission represents a larger portion of the total emission from the source (Fig. ??).

We find that this is a major limitation and inconsistency to all known SED fitting

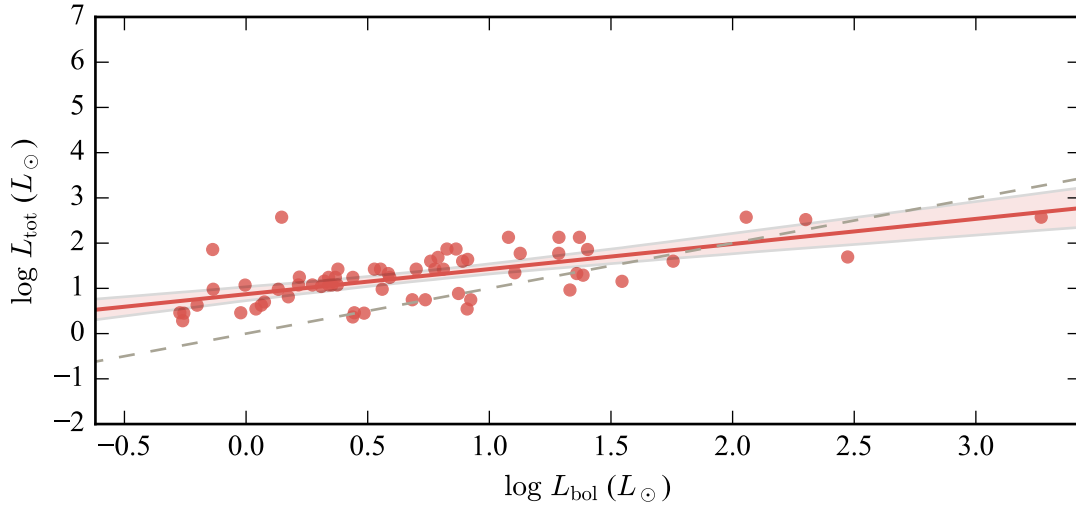


FIGURE II.12: Estimated luminosity vs bolometric luminosity. The best fit line is shown in red, along with 95% confidence intervals. The grey dashed line represents $L_{\text{tot}} = L_{\text{bol}}$. The excess modeled luminosity for smaller luminosities is caused by the external extinction, which absorbs a large fraction of the luminosity emitted by the central object but does not re-radiate it at longer wavelengths - this is one of the limitations of this exercise.

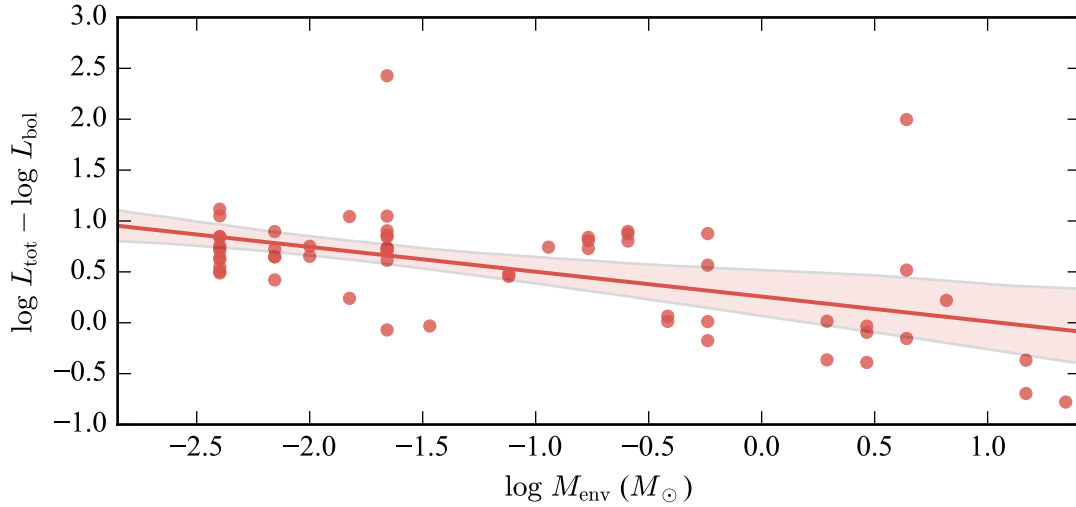


FIGURE II.13: Luminosity excess as a function of envelope mass.

methods. **Furlan:2016df** fit for extinction more than we do: they allow the external extinction to go up to $A_V = 40$ for some of their sources, and use all of the 2MASS bands in their fitting. It is not consistent to assume that so much dusty material is present along

the line of sight and only affect the short wavelengths, while not also being observed at longer wavelengths. Since the dust is optically thin at longer wavelengths, the far-infrared and submillimiter observations should account for this material which is obscuring the shortest wavelengths.

Our exploration with the fitting routine shows that limiting the external extinction helps by forcing more inclined geometries, where the light from the central star passes through the disk before reaching us. However, we were not able to account for the entirety of the short wavelength extinction by doing this, as the mid-infrared wavelength (IRAC and FORCAST bands) are also affected dramatically by more inclined geometries, which can compromise the fits. This could indicate a fundamental limit to our geometrical representation of YSOs.

For the clusters which do have submillimeter data points, the mass estimates are rather good, since these long-wavelengths points are constraining the mass along the line of sight very well. A summary of our fit results for Ophiuchus and NGC1333 is shown in Table II.17. Note that the luminosity that is used in this analysis is always the luminosity multiplied by the scaling factor s , under the assumption that the SED scales for small changes in luminosity. This scaling factor also represents a fundamental uncertainty in the distance measurement to our targets, as a distance error of 10% would cause a luminosity estimate that would differ by 20%.

7.4 Estimating parameter uncertainty

show uncertainties and discuss how they are determined show cross-correlation/cloud diagrams for a few targets

Plot fractional error of all fits

TABLE II.17: Fitted parameters for the three clusters where long-wavelength photometry is available.

SOFIA Name	Coordinates J2000	$R_{50}/R_{50,\text{cal}}$	α	R	M_{env} M_{\odot}	L_{tot} L_{\odot}	L_{bol} L_{\odot}	Inc. $^{\circ}$	Ext. %	β	γ
NGC1333.1	03h29m08s +31d21m57s	0.75	0.28	3.40	0.59 ± 0.3796	5.6 ± 3.12	8.38	0.0	12	0.0	
NGC1333.10	03h28m57s +31d14m15s	0.80	1.84	1.12	0.39 ± 0.2364	5.6 ± 1.69	4.82	18.7	14	0.0	
NGC1333.11	03h28m37s +31d13m30s	1.02	1.65	0.99	0.39 ± 0.1571	7.7 ± 1.37	7.47	18.7	12	0.0	
NGC1333.3	03h29m02s +31d20m21s	0.90	0.71	3.29	1.96 ± 0.8200	3.5 ± 0.80	8.10	0.0	14	0.0	
NGC1333.4	03h29m11s +31d18m31s	1.10	1.91	0.83	2.93 ± 0.5045	2.8 ± 0.42	3.06	18.7	14	1.0	
NGC1333.5	03h29m11s +31d18m20s	1.62	1.75	1.05	1.96 ± 0.3884	2.9 ± 1.00	2.79	18.7	9	1.0	
NGC1333.6	03h29m13s +31d18m14s	0.95	0.95	2.28	0.59 ± 0.1589	4.3 ± 1.72	1.16	18.7	14	1.0	
NGC1333.7	03h28m43s +31d17m35s	1.19	1.05	1.88	0.01 ± 0.0014	9.6 ± 2.16	1.36	50.8	0	0.0	
NGC1333.8	03h29m04s +31d16m04s	0.77	1.14	1.03	2.93 ± 1.1268	14.3 ± 2.24	35.11	0	12	1.0	
NGC1333.9	03h28m56s +31d14m37s	0.80	2.82	2.63	2.93 ± 0.5367	19.5 ± 3.67	24.28	18.7	14	1.0	
Oph.1	16h27m10s -24d19m13s	0.92	0.27	0.62	0.017 ± 0.0022	9.6 ± 1.80	3.63	65.1	4	0.0	
Oph.10	16h27m18s -24d28m55s	1.26	0.45	1.89	0.014 ± 0.0028	1.9 ± 0.38	0.55	61.7	14	1.0	
Oph.13	16h27m30s -24d27m43s	–	-0.39	3.46	0.014 ± 0.0023	6.5 ± 1.63	1.49	65.1	14	1.0	
Oph.14	16h27m28s -24d27m21s	1.89	-0.16	2.35	0.086 ± 0.0405	2.9 ± 0.78	0.95	18.7	14	1.0	
Oph.15	16h27m29s -24d39m17s	1.25	0.01	1.09	0.014 ± 0.0018	2.8 ± 0.59	0.55	54.6	12	0.0	
Oph.16	16h26m24s -24d24m48s	1.80	-0.74	1.49	0.011 ± 0.0008	17.7 ± 4.70	1.66	74.7	9	0.0	
Oph.17	16h26m24s -24d24m39s	0.96	-0.11	1.00	0.011 ± 0.0017	4.3 ± 0.88	0.63	77.8	14	0.0	
Oph.18	16h26m17s -24d23m45s	1.18	0.57	1.15	0.02 ± 0.0040	1.3 ± 0.21	0.22	65.1	14	0.0	
Oph.19	16h26m30s -24d23m00s	2.51	0.53	1.15	0.014 ± 0.0020	3.5 ± 0.74	1.10	58.2	13	0.0	
Oph.2	16h26m44s -24d34m48s	0.93	0.83	2.08	0.014 ± 0.0015	5.0 ± 0.97	1.19	77.8	14	1.0	
Oph.3	16h27m09s -24d37m18s	0.99	0.57	1.54	0.017 ± 0.0022	59.5 ± 11.99	13.39	37.9	10	0.0	
Oph.5	16h27m07s -24d38m15s	1.31	0.35	1.74	0.014 ± 0.0021	2.9 ± 0.66	0.53	68.4	14	1.0	
Oph.6	16h27m16s -24d38m46s	1.29	2.39	0.83	0.014 ± 0.0031	9.6 ± 3.41	0.73	90.0	12	0.0	
Oph.7	16h27m28s -24d39m34s	0.97	1.35	1.57	0.032 ± 0.0043	26.6 ± 4.90	6.47	74.7	14	0.0	
Oph.8	16h27m37s -24d30m35s	1.02	0.55	1.06	0.017 ± 0.0023	26.6 ± 5.15	5.00	80.9	14	0.0	
Oph.9	16h27m22s -24d29m54s	–	0.49	2.08	0.011 ± 0.0005	11.8 ± 2.71	0.99	80.9	14	0.0	

7.5 Discussion

External heating; over-simple geometry; non-uniform distribution of inclination angles.

Variability;

Extinction / inclination angle However, its interpretation is complicated. Extinction mostly affect the short wavelengths (after which the emission becomes optically thin, as

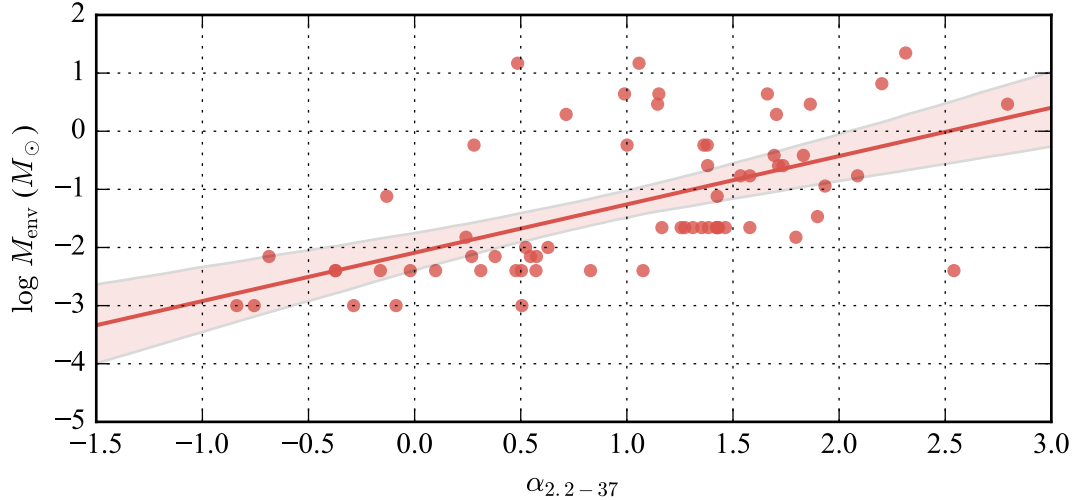


FIGURE II.14: Mass versus spectral index.

discussed in the introduction), but it still represents a column density of material which needs to be accounted for. For example, if a model is well fit with a low envelope mass but a high extinction (suggesting that it could be a small core with a large foreground extinction), the signature of the mass that is responsible for this extinction should be visible at long wavelengths as well. Because the dust is optically thin, the far-infrared and submillimeter wavelength measurements see the integrated emission along the line of sight. When using these fluxes to fit a model, they will most often strongly influence the mass inferred from the fit. But if the model still needs more extinction to account for the short wavelength fluxes, it suggests that the geometry is not properly modeled.

8 Application to two clusters

In our sample, we focus our attention on IRAS 20050+2720 and NGC 2071 that show very clustered sources which are resolved for the first time in the mid-IR with our observations with FORCAST. The fields that were observed are shown in Fig. ??, superimposed with

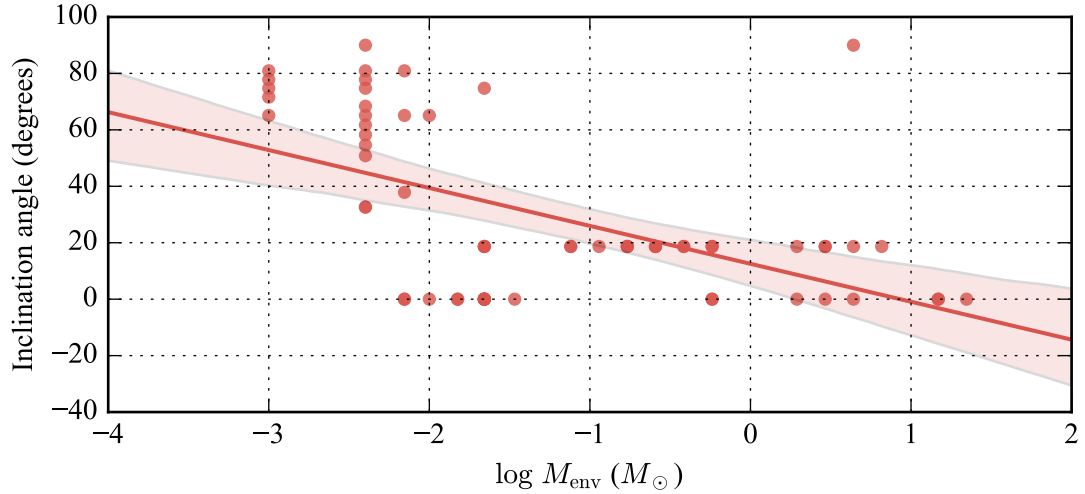


FIGURE II.15: Inclination versus mass.

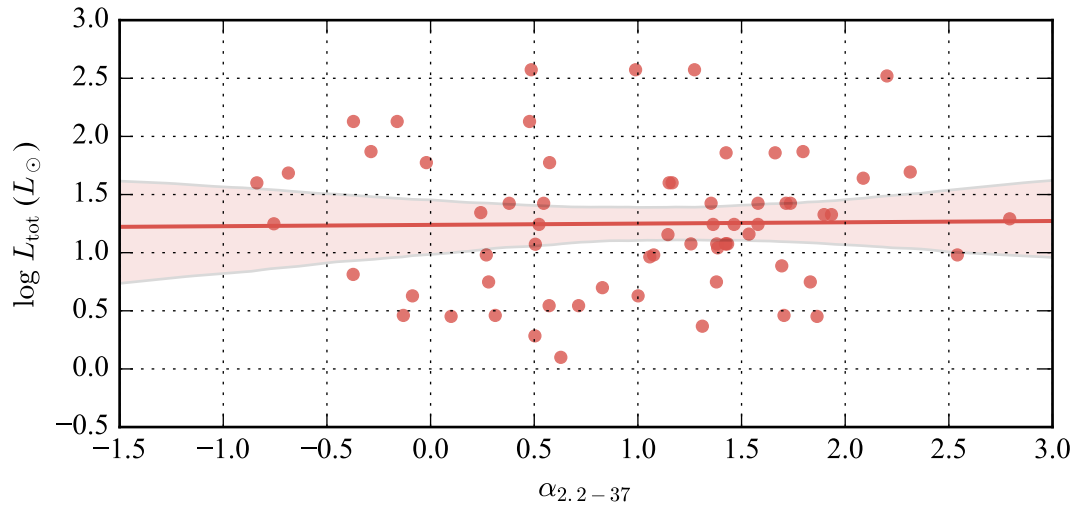


FIGURE II.16: Luminosity versus spectral index.

IRAC 3-color images to provide some context.

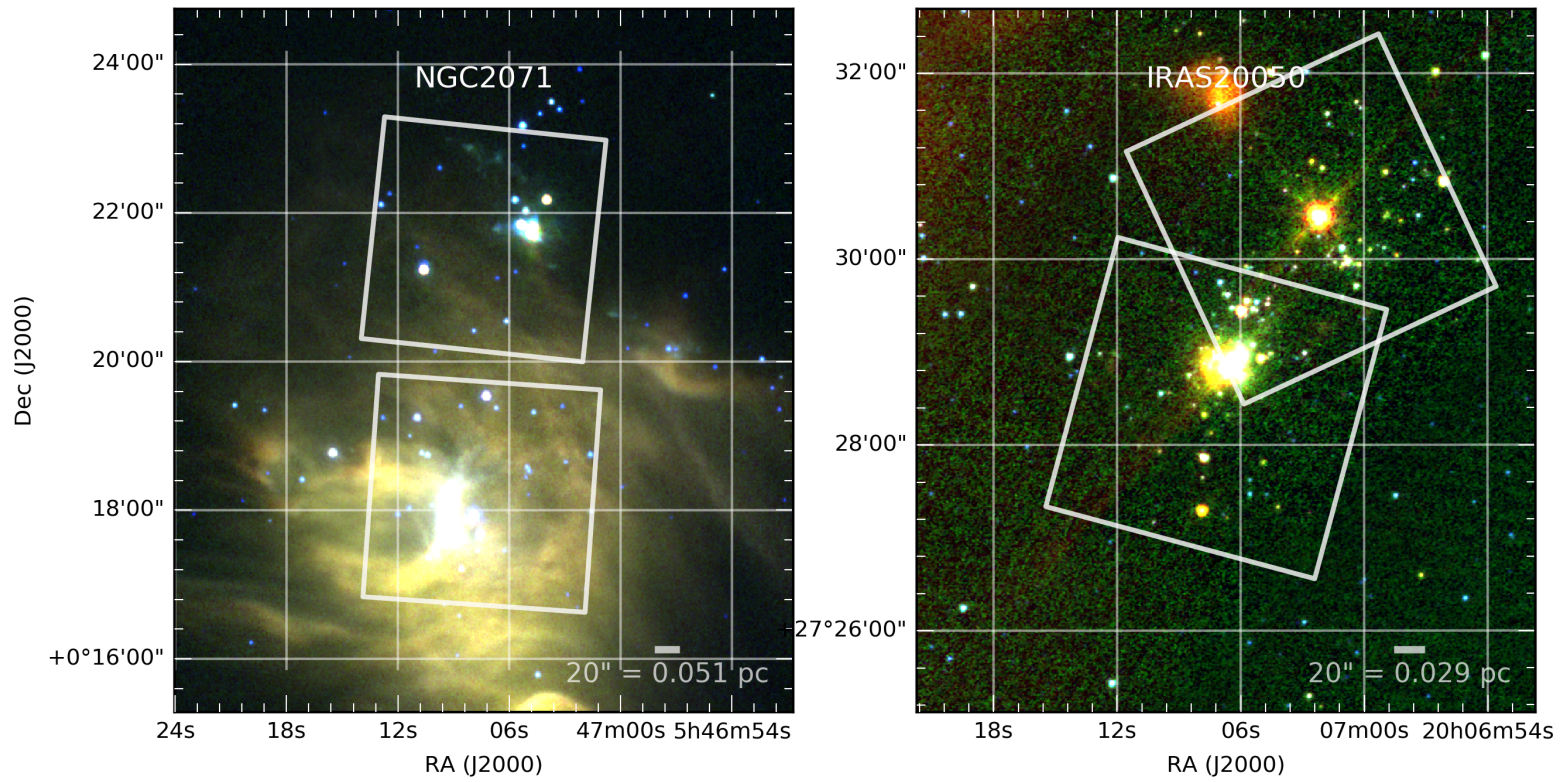


FIGURE II.17: IRAC 3-color images of NGC2071 and IRAS20050+2720.

8.1 IRAS20050+2720

8.1.1 Context

IRAS 20050+2720 is part of an active site of intermediate-mass star formation in the Cygnus Rift located at 700 pc (Wilking et al., 1989), with the particularity that it doesn't seem to contain any massive stars (Günther et al., 2012). The main cluster core is associated with water and methanol masers (Palla et al., 1991; Fontani, Cesaroni, and Furuya, 2010) and multipolar molecular outflows observed at millimeter wavelengths (Bachiller, Fuente, and Tafalla, 1995; Anglada et al., 1998; Beltrán et al., 2008), suggesting that the region might have experienced a recent episode of star formation in the past 0.1 Myr which contrasts with the average age of the cluster of 1 Myr (Chen et al., 1997; Gutermuth et al., 2005). Gutermuth et al., 2009 have identified > 170 YSOs surrounding the core and measured their continuum fluxes up to $8\mu\text{m}$ with IRAC. While measurements at longer wavelengths were able to provide estimates of the total luminosity of the cluster (e.g. using IRAS, Molinari et al., 1996, $388L_\odot$), the measurements are confused in the densest region and it has not been possible to properly associate the far-IR emission with its short wavelength counterpart because of the small separation between IRAC-detected protostars. The IRAS point source was classified as a luminous class 0 protostar (Bachiller, 1996), and its emission associated with the bright millimeter source MMS1 to the northwest of the core (Chini et al., 2001). Beltrán et al. (2008) show strong evidence that this region has multiple generations of stars, and suggest that a group of low-mass stars first completed its main accretion phase, before setting the stage for the birth of new intermediate-mass stars at the core of this cluster.

8.1.2 Observations and discussion

We have observed two fields within the cluster (see Fig. ??), including the brightest core at $20^h07^m06.70^s + 27^\circ28'54.5''$. Multiple sources in the core can be distinguished in the IRAC maps, but the core appears extended in *Spitzer* MIPS at 24 μm , and is identified as a single source with WISE. No high resolution far-infrared continuum data longward of 24 μm was available for this source. To our knowledge, our observations are the only mid-IR observations available that can properly resolve the various components of the dense region.

TABLE II.19: Sources fluxes (Jy) in IRAS 20050+2720.

SOFIA name	Coordinates J2000	ks	i1	i2	i3	i4	F11	F19	F31	F37
		Jy	Jy	Jy	Jy	Jy	Jy	Jy	Jy	Jy
IRAS20050.1	20h07m06.6s +27d28m48.0s	0.214 \pm 0.021	0.489 \pm 0.049	0.57 \pm 0.057	0.731 \pm 0.073	0.858 \pm 0.086	0.64 \pm 0.07	1.93 \pm 0.20	4.50 \pm 0.35	6.32 \pm 0.59
IRAS20050.2	20h07m06.2s +27d28m49.1s	0.002 \pm 0.002	0.041 \pm 0.004	0.142 \pm 0.014	0.264 \pm 0.026	0.308 \pm 0.031	0.06 \pm 0.06	1.45 \pm 0.19	9.31 \pm 0.72	11.96 \pm 1.19
	20h07m06.3s +27d28m56.6s	0.028 \pm 0.003	0.09 \pm 0.009	0.218 \pm 0.022	0.339 \pm 0.034	0.429 \pm 0.043	0.18 \pm 0.06	2.58 \pm 0.27	12.53 \pm 0.94	19.34 \pm 1.41
IRAS20050.4	20h07m05.9s +27d28m59.2s	0.002 \pm 0.002	0.023 \pm 0.003	0.039 \pm 0.004	0.053 \pm 0.008	0.055 \pm 0.008	0.06 \pm 0.05	0.25 \pm 0.20	8.54 \pm 0.80	12.85 \pm 1.25
	20h07m06.6s +27d28m53.1s	0.042 \pm 0.004	0.118 \pm 0.012	0.176 \pm 0.018	0.235 \pm 0.024	0.32 \pm 0.032	0.19 \pm 0.05	1.03 \pm 0.21	2.97 \pm 0.33	5.65 \pm 0.65
IRAS20050.6	20h07m02.2s +27d30m26.0s	0.155 \pm 0.016	0.537 \pm 0.054	0.771 \pm 0.077	1.113 \pm 0.111	1.805 \pm 0.181	1.81 \pm 0.13	2.29 \pm 0.17	1.64 \pm 0.14	1.22 \pm 0.38
	20h07m07.9s +27d27m15.8s	0.002 \pm 0.002	0.004 \pm 0.004	0.024 \pm 0.002	0.06 \pm 0.006	0.072 \pm 0.007	0.06 \pm 0.05	0.11 \pm 0.06	1.15 \pm 0.14	2.09 \pm 0.31

We distinguish 5 sources which appear to share an envelope at 37 μm . These sources are labeled in Fig. ???. IRAS20050.4 is coincident with the source at the northwestern end of the region, which is name OVRO1 in Beltrán et al. (2008). Two more sources are identified with these contours, to the south and east of OVRO1, but they do not appear

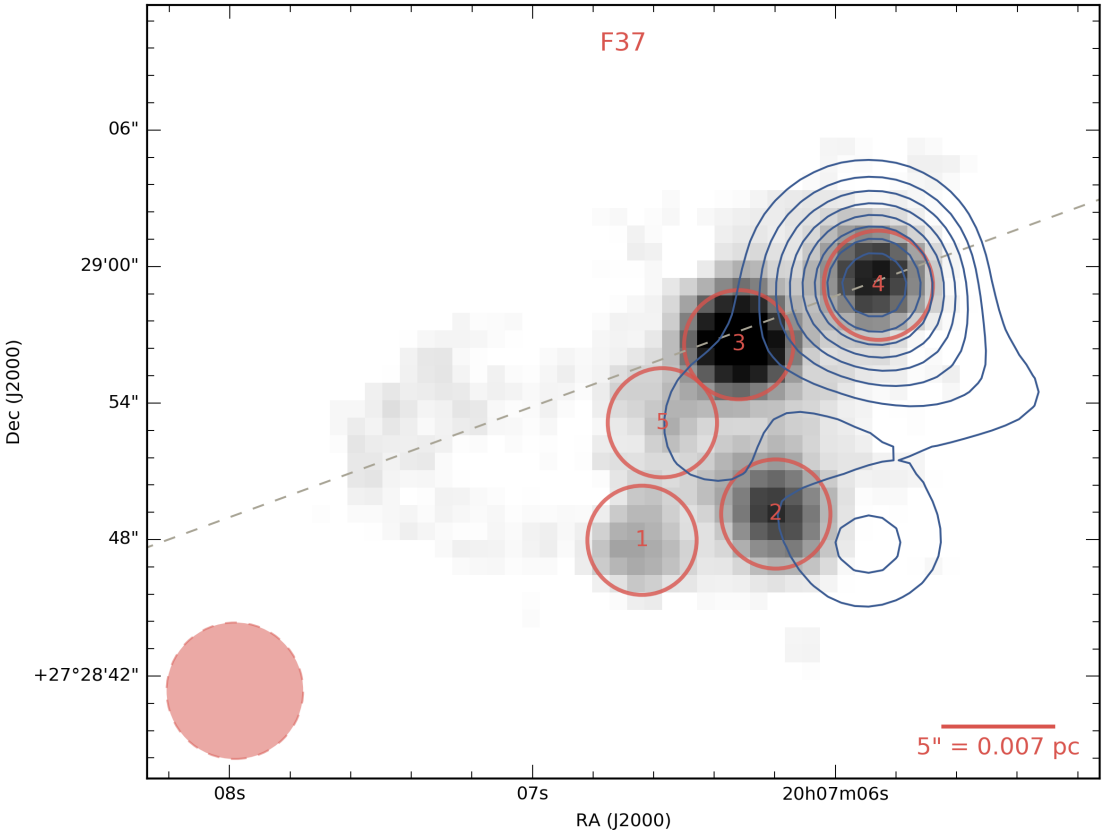


FIGURE II.18: 37 μm observations of the IRAS 20050+2720 core, with the 5 identified objects. The blue contours are from a 2.7 mm continuum emission observed by the OVRO array (Beltrán et al., 2008) at levels from 10 to 46 mJy beam⁻¹ by increments of 4 mJy beam⁻¹. The resolution of the 2.7 mm beam is $\sim 4.8''$, while the r.m.s noise is 1.5 mJy beam⁻¹. The dashed line is the axis of a bipolar outflow identified by Bachiller, Fuente, and Tafalla (1995). The beam shown at the bottom left represents the resolution of the FORCAST instrument.

to correlate with our SOFIA sources. The outflow axis (Outflow "A", Bachiller, Fuente, and Tafalla, 1995) appears to be aligned with extended emission that is visible to the east of the 5 sources. This extended emission is visible in both IRAC and FORCAST, and could be coinciding with CO velocity maps from Beltrán et al. (2008) showing blueshifted gas. The emission, totalling ~ 6 Jy at $37\text{ }\mu\text{m}$, appears diffuse and not connected to any particular YSO: this requires a mechanism to keep the dust emitting at these wavelengths, since no viable heating source is available to heat this material at these distances (many thousands of au from the nearest YSO).

Since the emission appears associated with the outflow, one possible scenario is that the material was recently ejected from the central clump of YSOs by this powerful outflow. This could be material from the diffuse envelope which seem to surround the 5 sources, or material from one given YSO's gravitationally bound envelope. The gas and dust being ejected at high velocities (Bachiller, Fuente, and Tafalla, 1995), it might not yet have time to completely thermalize with the surrounding medium (at which point it would not emit at these wavelengths). This scenario could be confirmed with high sensitivity submillimeter maps of the region, with a focus on dense gas tracers that would follow the mass in these regions. The existing maps from Beltrán et al. (2008) do not have sufficient sensitivity or resolution to properly identify the velocity field from the gas associated with this continuum emission.

Another possible explanation for this emission is that the gas and dust ejected from the cluster is heated by colliding with cold material in the surrounding medium. This could explain the bullet-like shape of the emission, and makes sense given the very high velocities from the outflow. The emission could arise from a supersonic shock layer that heats up the dust to a few hundreds of K, at which point its emission could become visible

in the IRAC and SOFIA bands.

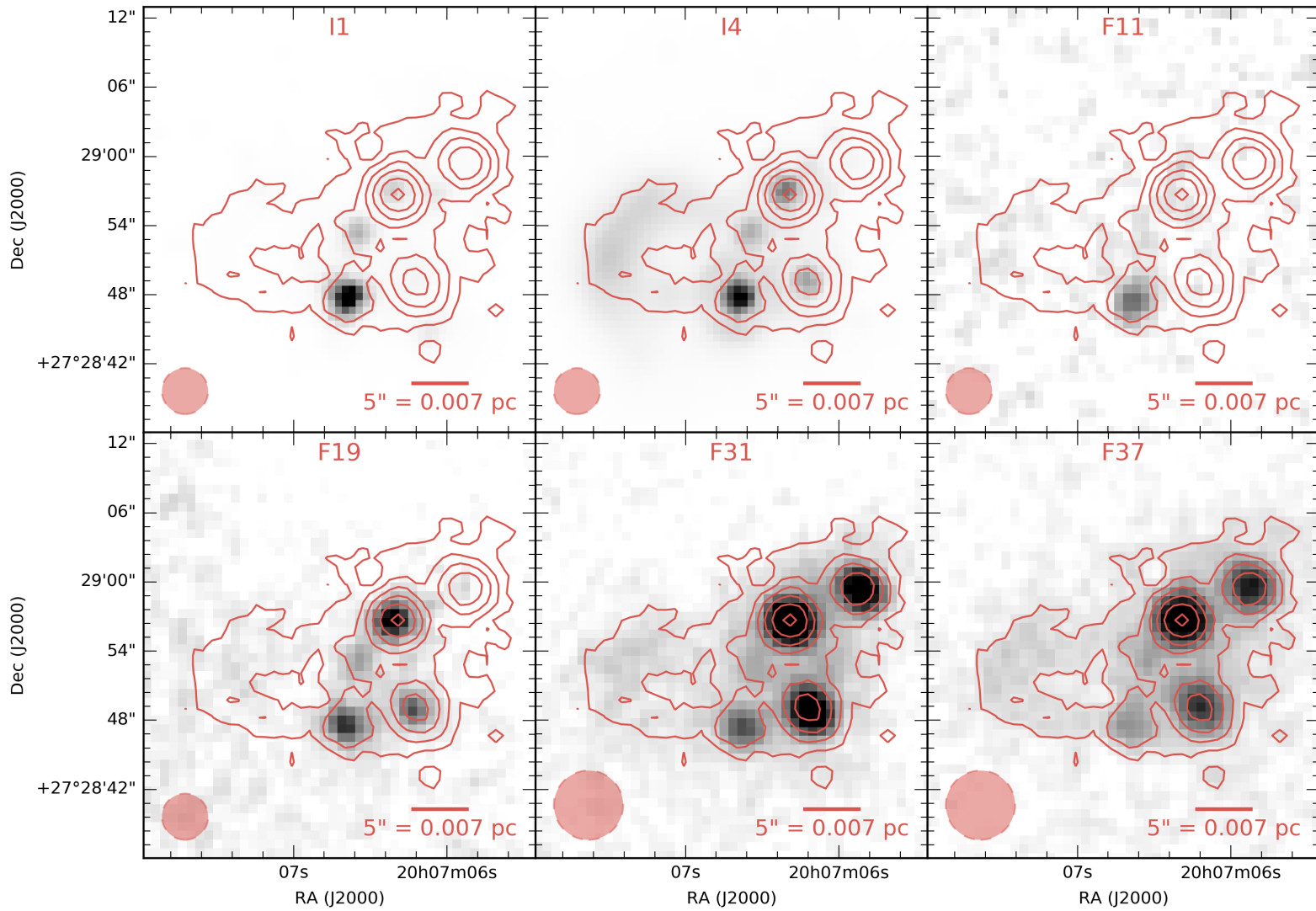


FIGURE II.19: The core of IRAS20050+2720 is seen in the four bands of the *Spitzer* IRAS instrument, as well as with the four FORCAST bands. The increased resolution of FORCAST compared to previous instruments allows to match the long-wavelength emission with its short wavelength counterpart. The stretch in each image is adjusted for optimal readability. The white contours correspond to the FORCAST 37 μm emission [mention the contour levels].

The 5 sources in the densest part of the cluster are all highly extincted based on the slopes of the emission in the 2MASS bands and the depth of the 10 μm silicate absorption feature (Fig. ??). IRAS20050.1 has a flat spectrum out to 37 μm , unlike the four other sources which are rising. IRAS20050.4 is the most steeply rising source, and is barely detected in the IRAC bands, suggesting that it is the most embedded source, which is corroborated by the fact that it is coincident with the strongest millimeter source in the region.

In testing the various scenarios of star formation, it is useful to obtain a measure of how much mass is available for the YSOs to grow after their original collapse. For this, clustered regions such as this one are an ideal laboratory since the YSOs usually appear to share an envelope. In this cluster, the typical separation between the sources are 6"-8", which correspond to projected distances of 3000-5600 au. This strongly indicates that the envelopes of individual YSOs are interacting with each other.

However, appropriately measuring the flux from each individual source in these clustered regions is challenging, since the sources are so close together. With an aperture of 2.4" (3 pixel radius), we managed to put non-overlapping apertures for all the 5 sources in IRAS 20050+2720. but since the aperture correction was derived considering a "total flux" aperture to be \sim 12 pixel radius, we are accounting for the same flux multiple times, even if the apertures are not overlapping. If we estimate the 37 μm flux from the eastern extended emission to be totalling \sim 5 Jy, we obtain about 22% of excess 37 μm flux when comparing the sum of the point sources and the total emission from the cluster (see Table II.23). At 31 μm , the flux excess is only about 10%. At 19 μm and below, the extended emission is within the noise uncertainty of the map.

This excess flux can only partially be explained by the tails of the PSF extending

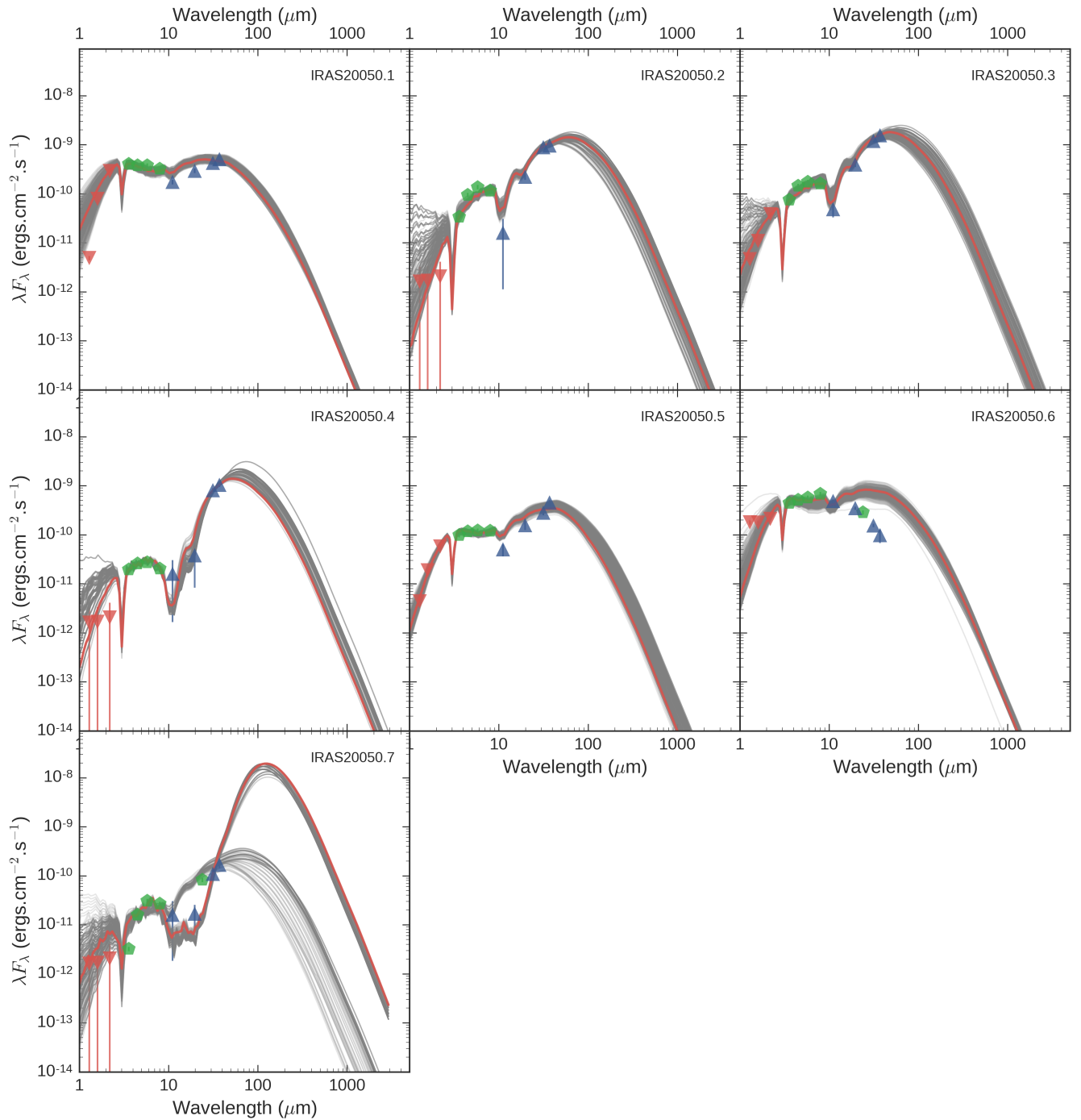


FIGURE II.20: SEDs of the 7 sources in the two fields.

well below the aperture size (see Fig. ??), with 10-15% of the total energy still existing in the annulus outward of 8 pixels ($6''$) from the aperture center. However, the contribution of a source to any given other source is only a fraction of this since it would only correspond to the amount of flux within a 3-pixel aperture. We conclude that the PSF shape is not responsible for the observed excess flux at both wavelengths.

One possible explanation would be that diffuse thermal emission occurs across the entire region. This could be caused by heating internal to the cluster (powered by the outflow, for example, like the eastern extended emission) or by a population of stochastically heated very small grains, which are not in LTE. The high outflow activity in this region could carve out multiple cavities which facilitate heating from the individual stars to extended over to larger distances within the envelopes and the shared mass reservoir. At $37\text{ }\mu\text{m}$, the level of diffuse emission required to account for the excess flux is about $0.05\text{ Jy pixel}^{-1}$, which is the same as the average diffuse emission in the eastern region. Such an explanation would also help account for the high amount of external extinction that is needed to fit most of the SEDs in this region.

This tends to favor a scenario where protostars are fragmenting from a cloud and continue accreting material within that original envelope. The envelopes of neighboring YSOs interact, and possibly can exchange material as some YSOs become more massive (competitive accretion).

8.2 NGC 2071

8.2.1 Context

The NGC 2071 star-forming region is one of several active areas of star formation in the northern part of L1630 giant molecular cloud which is located at a distance of 422 pc

TABLE II.21: Clustered sources in the densest region of IRAS20050.

SOFIA name	F11 Jy	F19 Jy	F31 Jy	F37 Jy
IRAS20050.1	0.64	1.93	4.50	6.32
IRAS20050.2	0.06	1.45	9.31	11.96
IRAS20050.3	0.18	2.58	12.53	19.34
IRAS20050.4	0.06	0.25	8.54	12.85
IRAS20050.5	0.19	1.03	2.97	5.65
Sum of point sources in cluster	1.13	7.24	37.84	56.11
Total cluster emission	1.79	7.07	37.36	49.33
Ratio	1.58	0.98	0.99	0.88

([vanDishoeck:2011em](#)). NGC 2071 itself is a reflection nebula. The NGC 2071 infrared cluster, located about 4' north of the reflection nebula, is a region of intermediate mass star formation (Strom, Strom, and Vrba, 1976; Persson et al., 1981; Butner et al., 1990). Maps of the cloud in CO and its isotopomers (Buckle et al., 2010) show a large scale clump with $\sim 1000 M_{\odot}$ associated with the cluster. Dust continuum emission at $\lambda=0.85$ and 1.3 mm peaks on center of the cluster extending 1' in diameter containing $30 M_{\odot}$ of gas and dust (Johnstone et al., 2001; Mitchell et al., 2001; Launhardt et al., 1996). Emission from CS in the J=2-1 through J=7-6 indicate that the gas in this region is centrally condensed with a density of $\sim 1 \times 10^6 \text{ cm}^{-3}$ (Zhou, Evans, and Mundy, 1990).

There are a number of near infrared surveys of the young cluster (e.g., Strom, Strom, and Vrba, 1976; Lada et al., 1991; Megeath et al., 2012; Spezzi et al., 2015). Spezzi et al., 2015 identify 52 YSOs associated with the NGC 2071 cluster, with the majority Class II sources. Flaherty and Muzerolle, 2008 estimate an age of ~ 2 Myr for the cluster, consistent with the large fraction of Class II sources (Evans et al., 2009. The brightest far infrared emission from the cluster is associated with the IRS1 region (Harvey et al., 1979; Butner et al., 1990), which has an estimated total luminosity of $520 L_{\odot}$. The immediate region of

IRS 1 is, in fact, home to a number of YSOs that are infrared, X-ray, and radio sources (Skinner et al., 2009; Carrasco-González et al., 2012; van Kempen et al., 2012). The radio (Carrasco-González et al., 2012) and H₂ emission line imaging indicate that IRS 1, IRS 2, IRS 3, and, perhaps, VLA 1 are YSOs with outflows. The larger scale molecular outflow associated with this region is well studied in a number of molecules (Bally, 1982; Chernin and Masson, 1993; Stojimirović, Snell, and Narayanan, 2008).

Figure ?? shows the Spitzer 3.1 μm image of the IRS 1 region on the left (image from Spitzer Archive: Megeath et al., 2012) and the Herschel 70 μm image on the right (image from Herschel Archive: Gould Belt Project, P.I. André). The plus marks in both panels indicate the position of the brighter YSOs: IRS 1, IRS 2, IRS 3, IRS 4, and VLA 1. The inner red circle with a diameter of 26'' indicates the extend of the saturated region in the Spitzer MIPS 24 μm image; the outer red circle, diameter 60'', encompasses the region with strong imaging artifacts in the MIPS 24 μm image. The right panel shows Herschel 70 μm image which does not resolve the emission from IRS 1, IRS 2, IRS 3, and VLA 1. The centroid of the 24 μm and 70 μm emission is between IRS 1 and VLA 1 indicating that several of the sources are contributing to the total observed emission. Interferometric observations show that the millimeter wavelength dust emission is dominated by envelopes associated with IRS 1 and IRS 3, with estimated masses of 8.2 and 12.3 M_⊙ material, respectively (van Kempen et al., 2012). The millimeter emission also reveals the presence of disks with radii ≤ 100 au associated with IRS 1 and IRS 3 (van Kempen et al., 2012).

The luminosities and masses of the individual source, IRS 1, IRS 2, IRS 3, and VLA 1, are not known. The Spectral Energy Distributions (SEDs) shortward of 10 μm support their identification as embedded YSOS (Skinner et al., 2009). Skinner et al., 2009 gives a clear discussion of the possibilities for IRS 1 and concludes that it is likely a mid-to

late B star. van Kempen et al., 2012 find luminosities of 10, 3.4, and $\leq 27 L_{\odot}$ for IRS 1, 2, and 3, respectively, and stellar masses of $\leq 1 M_{\odot}$ for each, based on SED fitting. These masses and luminosities are not consistent with estimate of the total luminosity of the region of $520 L_{\odot}$ (Butner et al., 1990). The far infrared images from Herschel reveal that IRS 1 alone does not totally dominate, as seen in Fig. ??; IRS 1, VLA 1, and IRS 3 likely make substantial contributions to the emission with lesser emission from IRS 2 and IRS 4.

8.2.2 Observations and discussion

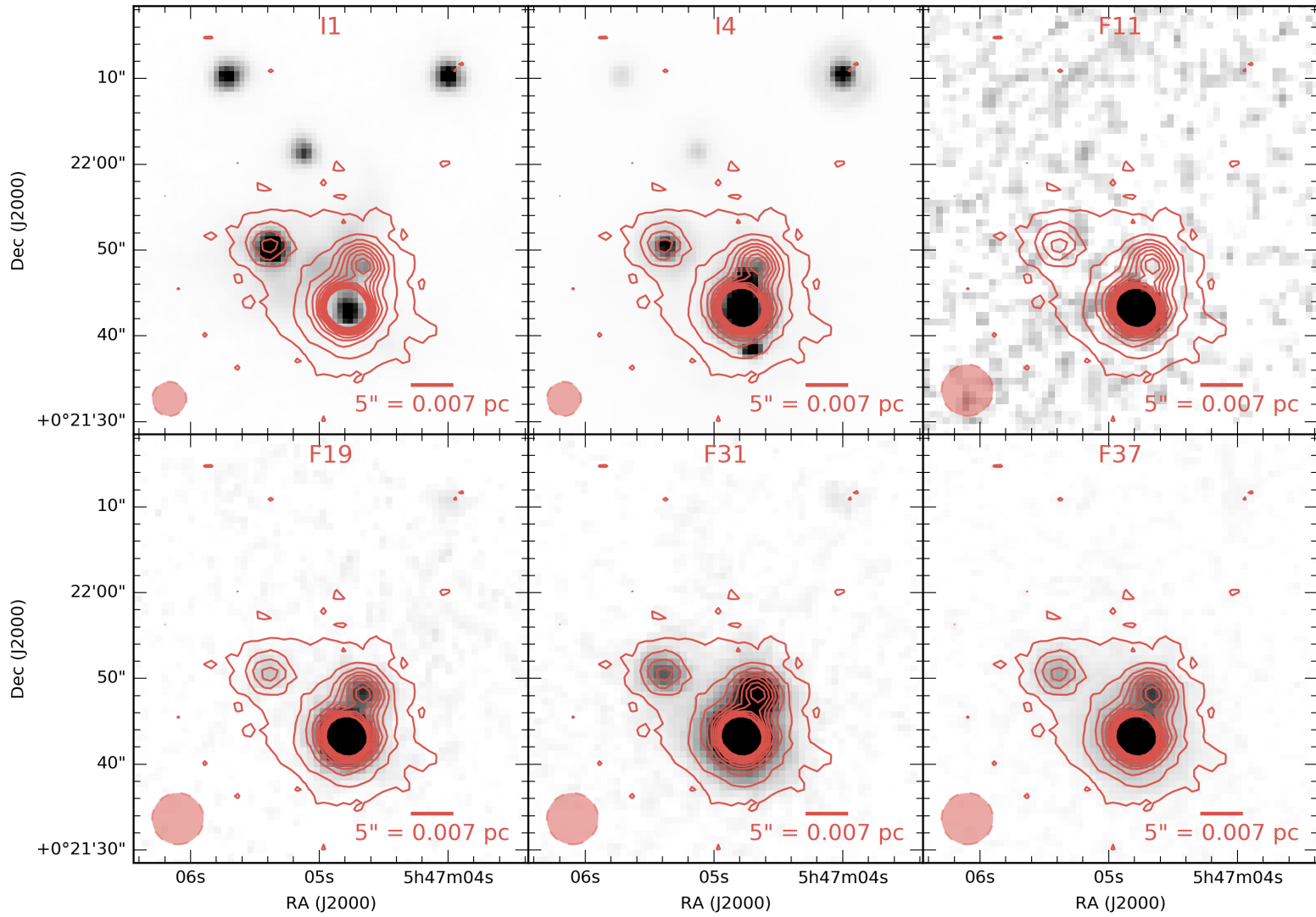


FIGURE II.21: The core of NGC2071 is seen in two bands of the *Spitzer* IRAC instrument ("I1" and "I4"), as well as with the four FORCAST bands. The increased resolution of FORCAST compared to previous instruments allows to match the long-wavelength emission with its short wavelength counterpart. The stretch in each image is adjusted for optimal readability.

The white contours correspond to the FORCAST 37 μm emission [mention the contour levels].

TABLE II.23: Sources in the densest region of NGC2071.

SOFIA name	F11 Jy	F19 Jy	F31 Jy	F37 Jy
NGC2071.1	10.07	72.041	167.93	234.93
NGC2071.2	0.38	11.207	56.70	89.55
NGC2071.3	0.19	3.027	19.97	37.56
Sum of point sources in cluster	10.65	86.28	244.61	362.03
Total cluster emission	13.523	94.16	280.14	362.99
Ratio	1.27	1.09	1.15	1.00

Show sum of sources compared to cluster total

9 Conclusion and future work

Spatial extension

Bibliography

- Allamandola, L J, A G G M Tielens, and J R Barker (1985). “Polycyclic aromatic hydrocarbons and the unidentified infrared emission bands - Auto exhaust along the Milky Way”. In: *Astrophysical Journal* 290, pp. L25–L28.
- Allen, L et al. (2007). “The Structure and Evolution of Young Stellar Clusters”. In: *Protostars and Planets V*, p. 361.
- Anglada, Guillem et al. (1998). “On the Exciting Sources of the L723 and IRAS 20050+2720 Quadrupolar Molecular Outflows”. In: *Star Formation with the Infrared Space Observatory* 132, p. 303.
- Astropy Collaboration et al. (2013). “Astropy: A community Python package for astronomy”. In: A&A 558, A33, A33. DOI: 10.1051/0004-6361/201322068. arXiv: 1307.6212 [astro-ph.IM].
- Bachiller, R, A Fuente, and M Tafalla (1995). “An extremely high velocity multipolar outflow around IRAS 20050 + 2720”. In: *Astrophysical Journal* 445, pp. L51–L54.
- Bachiller, Rafael (1996). “Bipolar Molecular Outflows from Young Stars and Protostars”. In: *Annual Review of Astronomy and Astrophysics* 34.1, pp. 111–154.
- Bally, J. (1982). “Energetic activity in a star-forming molecular cloud core - A disk constrained bipolar outflow in NGC 2071”. In: ApJ 261, pp. 558–568. DOI: 10.1086/160366.
- Beltrán, M T et al. (2008). “On the nature of outflows in intermediate-mass protostars: a case study of IRAS 20050+2720”. In: *Astronomy and Astrophysics* 481.1, pp. 93–105.

- Bonnell, I A et al. (1997). “Accretion and the stellar mass spectrum in small clusters”. In: *Monthly Notices of the Royal Astronomical Society* 285, p. 201.
- Bonnell, Ian A and Matthew R Bate (2002). “Accretion in stellar clusters and the collisional formation of massive stars”. In: *Monthly Notice of the Royal Astronomical Society* 336.2, pp. 659–669.
- (2006). “Star formation through gravitational collapse and competitive accretion”. In: *Monthly Notices of the Royal Astronomical Society* 370.1, pp. 488–494.
- Buckle, J. V. et al. (2010). “The JCMT Legacy Survey of the Gould Belt: a first look at Orion B with HARP”. In: MNRAS 401, pp. 204–222. DOI: [10.1111/j.1365-2966.2009.15619.x](https://doi.org/10.1111/j.1365-2966.2009.15619.x). arXiv: 0908.4162.
- Butner, H. M. et al. (1990). “High-resolution, far-infrared observations of NGC 2071”. In: ApJ 364, pp. 164–172. DOI: [10.1086/169398](https://doi.org/10.1086/169398).
- Cardelli, Jason A, Geoffrey C Clayton, and John S Mathis (1989). “The relationship between infrared, optical, and ultraviolet extinction”. In: *Astrophysical Journal* 345, pp. 245–256.
- Carrasco-González, C. et al. (2012). “Multiplicity, Disks, and Jets in the NGC 2071 Star-forming Region”. In: ApJ 746, 71, p. 71. DOI: [10.1088/0004-637X/746/1/71](https://doi.org/10.1088/0004-637X/746/1/71). arXiv: 1111.5469.
- Chen, H et al. (1997). “IRAS 20050+2720: An Embedded Young Cluster Associated with a Multipolar Outflow”. In: *The Astrophysical Journal* 475.1, pp. 163–172.
- Chernin, L. and C. Masson (1993). “Observations of SO and SiO in the outflow from NGC 2071”. In: ApJ 403, pp. L21–L24. DOI: [10.1086/186712](https://doi.org/10.1086/186712).
- Chini, R et al. (2001). “Mm/Submm images of Herbig-Haro energy sources and candidate protostars”. In: *Astronomy and Astrophysics* 369.1, pp. 155–169.

- Di Francesco, J et al. (2007). “An Observational Perspective of Low-Mass Dense Cores I: Internal Physical and Chemical Properties”. In: *Protostars and Planets V*, pp. 17–32.
- Dunham, Michael M et al. (2010). “Evolutionary Signatures in the Formation of Low-Mass Protostars. II. Toward Reconciling Models and Observations”. In: *The Astrophysical Journal* 710.1, pp. 470–502.
- Evans II, N. J. et al. (2009). “The Spitzer c2d Legacy Results: Star-Formation Rates and Efficiencies; Evolution and Lifetimes”. In: ApJS 181, 321, pp. 321–350. DOI: 10.1088/0067-0049/181/2/321. arXiv: 0811.1059.
- Evans, Neal J et al. (2009). “The Spitzer c2d Legacy Results: Star-Formation Rates and Efficiencies; Evolution and Lifetimes”. In: *The Astrophysical Journal Supplement* 181.2, pp. 321–350.
- Ferrière, Katia M (2001). “The interstellar environment of our galaxy”. In: *Reviews of Modern Physics* 73.4, pp. 1031–1066.
- Flaherty, K. M. and J. Muzerolle (2008). “Evidence for Early Circumstellar Disk Evolution in NGC 2068/71”. In: AJ 135, pp. 966–983. DOI: 10.1088/0004-6256/135/3/966. arXiv: 0712.1601.
- Fontani, F, R Cesaroni, and R S Furuya (2010). “Class I and Class II methanol masers in high-mass star-forming regions”. In: *Astronomy and Astrophysics* 517, A56.
- Gillett, F C, W J Forrest, and K M Merrill (1973). “8 - 13-micron spectra of NGC 7027, BD +30 3639, and NGC 6572.” In: *Astrophysical Journal* 183, pp. 87–93.
- Günther, H M et al. (2012). “IRAS 20050+2720: Anatomy of a Young Stellar Cluster”. In: *The Astronomical Journal* 144.4, p. 101.

- Gutermuth, R A et al. (2009). “A Spitzer Survey of Young Stellar Clusters Within One Kiloparsec of the Sun: Cluster Core Extraction and Basic Structural Analysis”. In: *The Astrophysical Journal Supplement* 184.1, pp. 18–83.
- Gutermuth, R A et al. (2011). “A Correlation between Surface Densities of Young Stellar Objects and Gas in Eight Nearby Molecular Clouds”. In: *The Astrophysical Journal* 739.2, p. 84.
- Gutermuth, Robert A et al. (2005). “The Initial Configuration of Young Stellar Clusters: A K-Band Number Counts Analysis of the Surface Density of Stars”. In: *The Astrophysical Journal* 632.1, pp. 397–420.
- Harvey, P. M. et al. (1979). “Infrared observations of NGC 2071/IRS/ and AFGL 490 - Two low-luminosity young stars”. In: ApJ 229, pp. 990–993. DOI: [10.1086/157033](https://doi.org/10.1086/157033).
- Herter, T L et al. (2012). “First Science Observations with SOFIA/FORCAST: The FORCAST Mid-infrared Camera”. In: *The Astrophysical Journal Letters* 749.2, p. L18.
- Herter, T L et al. (2013). “Data Reduction and Early Science Calibration for FORCAST, A Mid-Infrared Camera for SOFIA”. In: *Publications of the Astronomical Society of the Pacific* 125.933, pp. 1393–1404.
- Johnstone, D. et al. (2001). “Large Area Mapping at 850 Microns. III. Analysis of the Clump Distribution in the Orion B Molecular Cloud”. In: ApJ 559, pp. 307–317. DOI: [10.1086/322323](https://doi.org/10.1086/322323).
- Kempen, T A van et al. (2012). “The Small-scale Physical Structure and Fragmentation Difference of Two Embedded Intermediate-mass Protostars in Orion”. In: *The Astrophysical Journal* 751.2, p. 137.

- Kennicutt, R. C. and N. J. Evans (2012). “Star Formation in the Milky Way and Nearby Galaxies”. In: ARA&A 50, pp. 531–608. DOI: [10.1146/annurev-astro-081811-125610](https://doi.org/10.1146/annurev-astro-081811-125610). arXiv: [1204.3552](https://arxiv.org/abs/1204.3552).
- Kennicutt, Robert C and Neal J Evans (2012). “Star Formation in the Milky Way and Nearby Galaxies”. In: *Annual Review of Astronomy and Astrophysics* 50.1, pp. 531–608.
- Kim, Sang-Hee, P G Martin, and Paul D Hendry (1994). “The size distribution of interstellar dust particles as determined from extinction”. In: *Astrophysical Journal* 422, pp. 164–175.
- Lada, Charles J and Elizabeth A Lada (2003). “Embedded Clusters in Molecular Clouds”. In: *Annual Review of Astronomy & Astrophysics* 41.1, pp. 57–115.
- Lada, E. A. et al. (1991). “A 2.2 micron survey in the L1630 molecular cloud”. In: ApJ 371, pp. 171–182. DOI: [10.1086/169881](https://doi.org/10.1086/169881).
- Larson, R B (1994). “The Evolution of Molecular Clouds”. In: *The Structure and Content of Molecular Clouds* 439.Chapter 2, pp. 13–28.
- Launhardt, R. et al. (1996). “Dust emission from star-forming regions. IV. Dense cores in the Orion B molecular cloud.” In: A&A 312, pp. 569–584.
- Li, Aigen and B T Draine (2001). “Infrared Emission from Interstellar Dust. II. The Diffuse Interstellar Medium”. In: *The Astrophysical Journal* 554.2, pp. 778–802.
- Mathis, J S, W Rumpl, and K H Nordsieck (1977). “The size distribution of interstellar grains”. In: *Astrophysical Journal* 217, pp. 425–433.
- Mathis, John S (1990). “Interstellar dust and extinction”. In: IN: *Annual review of astronomy and astrophysics. Vol. 28 (A91-28201 10-90). Palo Alto* 28.1, pp. 37–70.

- McKee, Christopher F and Eve C Ostriker (2007). “Theory of Star Formation”. In: *Annual Review of Astronomy and Astrophysics* 45.1, pp. 565–687.
- McKee, Christopher F and Jonathan C Tan (2003). “The Formation of Massive Stars from Turbulent Cores”. In: *The Astrophysical Journal* 585.2, pp. 850–871.
- Megeath, S. T. et al. (2012). “The Spitzer Space Telescope Survey of the Orion A and B Molecular Clouds. I. A Census of Dusty Young Stellar Objects and a Study of Their Mid-infrared Variability”. In: AJ 144, 192, p. 192. DOI: 10.1088/0004-6256/144/6/192. arXiv: 1209.3826.
- Mitchell, G. F. et al. (2001). “A Submillimeter Dust and Gas Study of the Orion B Molecular Cloud”. In: ApJ 556, pp. 215–229. DOI: 10.1086/321574.
- Molinari, S et al. (1996). “A search for precursors of ultracompact HII regions in a sample of luminous IRAS sources. I. Association with ammonia cores.” In: *Astronomy and Astrophysics* 308, pp. 573–587.
- Myers, P C and E F Ladd (1993). “Bolometric temperatures of young stellar objects”. In: *Astrophysical Journal* 413, pp. L47–L50.
- Myers, Philip C (2011). “Star Formation in Dense Clusters”. In: *The Astrophysical Journal* 743.1, p. 98.
- Offner, Stella S R and Christopher F McKee (2011). “The Protostellar Luminosity Function”. In: *The Astrophysical Journal* 736.1, p. 53.
- Ossenkopf, V and Th Henning (1994). “Dust opacities for protostellar cores”. In: *Astronomy and Astrophysics (ISSN 0004-6361)* 291, pp. 943–959.
- Palla, F et al. (1991). “Water masers associated with dense molecular clouds and ultracompact H II regions”. In: *Astronomy and Astrophysics (ISSN 0004-6361)* 246, pp. 249–263.

- Persson, S. E. et al. (1981). “High Velocity h₂ Line Emission in the NGC2071 Region”. In: *ApJ* 251, p. L85. DOI: 10.1086/183699.
- Porras, Alicia et al. (2003). “A Catalog of Young Stellar Groups and Clusters within 1 Kiloparsec of the Sun”. In: *The Astronomical Journal* 126.4, pp. 1916–1924.
- Robitaille, T P (2011). “HYPERION: an open-source parallelized three-dimensional dust continuum radiative transfer code”. In: *Astronomy and Astrophysics* 536, A79.
- Robitaille, Thomas P et al. (2006). “Interpreting Spectral Energy Distributions from Young Stellar Objects. I. A Grid of 200,000 YSO Model SEDs”. In: *The Astrophysical Journal Supplement Series* 167.2, pp. 256–285.
- Robitaille, Thomas P et al. (2007). “Interpreting Spectral Energy Distributions from Young Stellar Objects. II. Fitting Observed SEDs Using a Large Grid of Precomputed Models”. In: *The Astrophysical Journal Supplement Series* 169.2, pp. 328–352.
- “Self-similar collapse of isothermal spheres and star formation” (1977). In: *Astrophysical Journal* 214, pp. 488–497.
- Sellgren, K (1994). “Tiny Grains, Large Molecules, and the Infrared Cirrus”. In: *The First Symposium on the Infrared Cirrus and Diffuse Interstellar Clouds. ASP Conference Series* 58, pp. 243–.
- Shirley, Yancy L et al. (2000). “Tracing the Mass during Low-Mass Star Formation. I. Submillimeter Continuum Observations”. In: *The Astrophysical Journal Supplement Series* 131.1, pp. 249–271.
- Skinner, S. L. et al. (2009). “Chandra and Spitzer Imaging of the Infrared Cluster in NGC 2071”. In: *ApJ* 701, pp. 710–724. DOI: 10.1088/0004-637X/701/1/710. arXiv: 0906.2428 [astro-ph.SR].

- Spezzi, L. et al. (2015). “The VISTA Orion mini-survey: star formation in the Lynds 1630 North cloud”. In: *ArXiv e-prints*. arXiv: 1505.04631 [astro-ph.SR].
- Stecher, T P and B Donn (1965). “On Graphite and Interstellar Extinction”. In: *Astro-physical Journal* 142, pp. 1681–.
- Stojimirović, I., R. L. Snell, and G. Narayanan (2008). “Multiple Parsec-Scale Outflows in the NGC 2071 Cluster”. In: *ApJ* 679, pp. 557–569. DOI: 10.1086/586688.
- Strom, K. M., S. E. Strom, and F. J. Vrba (1976). “Infrared surveys of dark-cloud complexes. I. The Lynds 1630 dark cloud.” In: *AJ* 81, pp. 308–313. DOI: 10.1086/111888.
- Terebey, S, F H Shu, and P Cassen (1984). “The collapse of the cores of slowly rotating isothermal clouds”. In: *Astrophysical Journal* 286, pp. 529–551.
- Ulrich, R K (1976). “An infall model for the T Tauri phenomenon”. In: *Astrophysical Journal* 210, pp. 377–391.
- van Kempen, T. A. et al. (2012). “The Small-scale Physical Structure and Fragmentation Difference of Two Embedded Intermediate-mass Protostars in Orion”. In: *ApJ* 751, 137, p. 137. DOI: 10.1088/0004-637X/751/2/137. arXiv: 1203.3718.
- Weingartner, Joseph C and B T Draine (2001). “Dust Grain-Size Distributions and Extinction in the Milky Way, Large Magellanic Cloud, and Small Magellanic Cloud”. In: *The Astrophysical Journal* 548.1, pp. 296–309.
- Whitney, B A et al. (2013). “Three-dimensional Radiation Transfer in Young Stellar Objects”. In: *The Astrophysical Journal Supplement* 207.2, p. 30.
- Whitney, Barbara A et al. (2003a). “2-D Radiative Transfer in Protostellar Envelopes: I. Effects of Geometry on Class I Sources”. In: *arXiv.org* 2, pp. 1049–1063. arXiv: astro-ph/0303479v1 [astro-ph].

- Whitney, Barbara A et al. (2003b). “Two-dimensional Radiative Transfer in Protostellar Envelopes. II. An Evolutionary Sequence”. In: *The Astrophysical Journal* 598.2, pp. 1079–1099.
- Wilking, B A et al. (1989). “A millimeter-wave spectral-line and continuum survey of cold IRAS sources”. In: *Astrophysical Journal* 345, pp. 257–264.
- Williams, J P, L Blitz, and C F McKee (2000). “The Structure and Evolution of Molecular Clouds: from Clumps to Cores to the IMF”. In: *Protostars and Planets IV (Book - Tucson: University of Arizona Press; eds Mannings,* pp. 97–.
- Yusef-Zadeh, F, M Morris, and R L White (1984). “Bipolar reflection nebulae - Monte Carlo simulations”. In: *Astrophysical Journal* 278, pp. 186–194.
- Zhou, S., N. J. Evans II, and L. G. Mundy (1990). “An NH₃ ring around the infrared sources in NGC 2071”. In: ApJ 355, pp. 159–165. DOI: 10.1086/168749.